

IGABEM of 2D and 3D liquid inclusions

Dai Rui, Dong Chunying*, Xu Chuang, Sun Deyong

Department of Mechanics, School of Aerospace Engineering, Beijing Institute of Technology, Beijing 100081, China



ARTICLE INFO

Keywords:
IGABEM
Liquid inclusion
Elastic matrix
Mechanical property

ABSTRACT

Randomly distributed liquid inclusions in elastic matrix exist in nature, biology, material science and other fields. In this paper, the isogeometric analysis boundary element method (IGABEM) is applied to study the mechanical properties of the elastic matrix with liquid inclusions, in which the liquid inclusion is assumed to be linearly compressible and the interface tension is neglected. Singularity subtraction technique (SST) and Tels transformation method are respectively used to solve the strongly and weakly singular integrals in two-dimensional (2D) problems, while the power series expansion method is used to carry out various singular integrals in three-dimensional (3D) problems. The oriented bounding box (OBB) is adopted to generate the randomly distributed liquid inclusions, which can be formed easily by the control points of the IGA. Numerical examples show the accuracy and effectiveness of the present method in the study of liquid inclusions.

1. Introduction

Materials containing liquid inclusions are widely found in nature [1, 2], biological tissues [3] and materials science [4, 5]. The mechanical properties of these materials have attracted the attention of many scholars. Wu et al. [6] studied the elastic field of a compressible elliptical liquid inclusion in two-dimensional (2D) infinite plane by analytical method, and the results showed that both the change of liquid pressure and the surface tension played an important role in reducing the stress concentration factor. Based on the framework of Eshelby [7], Chen et al. [8] derived the displacement and stress fields of the matrix under remote load and gave an explicit expression for spherical case. To identify when the liquid compressibility had a significant effect, Chen et al. [8] also studied the shape revolution of liquid inclusion and stress concentration factor of the matrix, and finally classified the liquid inclusion examples in nature and engineering. Considering the limitations of theoretical and experimental methods, some numerical methods, such as the finite element method (FEM) and boundary element method (BEM), are usually used to study these problems. The FEM is a very mature numerical algorithm, which has been widely used in solving various engineering problems. Wang et al. [9] developed a finite-element formulation accounting for surface tension and large deformations in three-dimensional (3D) settings, and showed the simulation capability by examining the problem of fluid-filled droplet in a soft solid matrix. Seifi et al. [10] presented a new finite deformation, dynamical finite element model to study the effect of surface tension on the deformation

of dielectric elastomers by three numerical examples. Although the FEM can solve liquid inclusion problem well, the meshing should be carried out in the whole area, which significantly affects the accuracy of the FEM and takes up lots of time in the analysis. The BEM is a semi-analytical numerical method based on boundary integral equation (BIE). It mainly has the following advantages comparing to the FEM: (1) It only discretizes the boundary, which can reduce the computation dimension; (2) It automatically satisfies the boundary conditions at infinity so that it is suitable for solving the infinite problems; (3) It has high accuracy, since the BEM adopts the analytical fundamental solutions. With the development of the BEM, it has been widely used to solve elastic problem [11], heat conduction problem [12], fracture problem [13], acoustic problem [14, 15]. Huang et al. [16] applied the BEM to the 2D solid with incompressible fluid-filled pores and computed the equivalent mechanical properties of the solid with randomly distributed fluid-filled pores. Ma et al. [17] used the eigenstrain boundary integral equation based on Eshelby's theory to study the 2D solid problem with fluid-filled pores, and the results showed that the method had high accuracy and efficiency. More research about liquid inclusions can be found in [18–22].

In the traditional numerical analysis process, the first stage is to establish an accurate geometric model in Computer Aided Design (CAD) software. Then the numerical analysis is carried out in Computer Aided Engineering (CAE) software. However, since CAD and CAE use different mathematical representations, it is necessary to transform the CAD model into a solvable model that can be used in CAE software, which

* Corresponding author.

E-mail address: cydong@bit.edu.cn (C. Dong).

significantly increases the computational cost. Therefore, in order to realize the seamless connection between CAD and CAE, Hughes et al. [23] developed the idea of isogeometric analysis (IGA) in 2005, which is the application of the non-uniform rational B-spline (NURBS) basis functions as the shape functions into the FEM analysis, called IGAFEM. The main advantages of IGA are as follows: (1) It accurately describes the geometry without the geometric discretization errors; (2) It saves the meshing time, and simplifies the refinement process by knot insertion and degree elevation; (3) The NURBS basis functions have high continuity. With the rapid development of the IGAFEM, it has been proved to be an efficient method in many fields [24,25].

Since both the BEM and IGA deal with the structure surfaces, it is natural to apply the IGA to BEM, called IGABEM. This idea was earlier proposed in [26–28] and later some scholars conducted a lot of research on the IGABEM. For example, Takahashi et al. [29] successfully applied the fast multipole method to the IGABEM for Laplace equation. Simpson et al. [30] introduced in detail the application of the IGABEM to 2D elastostatic problems. The IGABEM inherits the advantages of the IGA and traditional BEM, which not only maintains the accuracy of geometric description and saves the time of meshing, but also inherits the high accuracy of the traditional BEM. Afterwards, this method develops rapidly and is widely used in many fields, such as elastic problem [31], acoustic problem [32], heat conduction problem [33], crack problem [34], shape optimization [35], the FE-BE coupling method [36,37]. However, similar to the traditional BEM, there are some challenges in IGABEM. First, when the field point approaches the source point, different kinds of singular integrals will appear, which has a significant effect on the accuracy of the IGABEM. Therefore, some mature methods to deal with singular integrals have been proposed. For example, Simpson et al [30] adopted singularity subtraction technique (SST) [38] to solve the strongly singular integrals and Tolls transformation [39] to the weakly singular integrals. Gong et al. [40] successfully applied the power series expansion method [41] in IGABEM. Yang et al. [42] improved the power series expansion method so that it could be used for higher order NURBS in IGABEM. In addition, the coefficient matrices of IGABEM are fully populated and non-symmetric. Thus, when the degrees of freedom (DOFs) increase, the storage and computation will be difficult. To solve this problem, some fast-direct algorithms had been studied, such as fast multipole method (FMM) [43], adaptive cross approximation method (ACA) [44], and hierarchical matrix [45].

To the authors' knowledge, liquid inclusion problems using the IGABEM have not yet occurred. In this paper, the IGABEM is used to study the mechanical properties of 2D and 3D liquid inclusion problems. The content of the paper is organized as follows: Section 2 provides the description of the liquid inclusion problems with some assumptions and formulas. In Section 3, a brief introduction for the NURBS and the framework of IGABEM are presented. The numerical examples are shown in Section 4 and some conclusions are given in Section 5.

2. Problem description

The liquid inclusion problems refer to the randomly distributed liquid inclusions with arbitrary shapes embedded in 2D or 3D elastic matrix. In this paper, the IGABEM is used to study the mechanical properties of such problems. To reach this goal, we first discuss the elastic field of an infinite matrix containing an isolated liquid inclusion based on the IGABEM, and then investigate the mechanical properties of the problems of randomly distributed liquid inclusions in elastic matrix. Some assumptions and formulas are given in this section.

Assume that the liquid is linear compressible, and the surface effect at liquid-matrix interface is neglected. Then we can get [20]

$$-K \frac{\Delta V}{V} = p \quad (1)$$

where ΔV and V are the volume variation and the initial volume for 3D

problem, respectively. While for 2D problem, they represent the changed area and the initial area of the inclusion. K is the bulk modulus of the liquid and p is the pressure after load. At the liquid-matrix interface, the following formula [8] can be obtained

$$\sigma \cdot \mathbf{n} = -p\mathbf{n} \quad (2)$$

in which σ and \mathbf{n} are the stress and outer unit normal at the interface.

3. Formulation of the IGABEM

In this paper, we focus on the implementation of the IGABEM for the elastic field of liquid inclusion problems. Therefore, we briefly present some conclusions about IGA in the section 3.1, and more details can be found in [46]. From Section 3.2 to Section 3.4, we show some implementations of IGABEM for 3D problems, and the content for 2D plane strain problems can be obtained in Appendix A. In the Section 3.5, we will get the formula for solving the liquid inclusion problems in IGABEM.

3.1. NURBS

Before presenting NURBS basis functions, the B-spline basis functions are first introduced. The B-spline basis functions denoted by $N_{i,p}(\xi)$ with degree $p = 0$ at knot vector $U = \{\xi_0, \xi_1, \dots, \xi_n + p + 1\}$ are defined as follows:

$$N_{i,0} = \begin{cases} 1 & \text{if } \xi_i \leq \xi < \xi_{i+1} \\ 0 & \text{otherwise} \end{cases} \quad (3)$$

The higher order basis functions can be obtained by

$$N_{i,p}(\xi) = \frac{\xi - \xi_i}{\xi_{i+1} - \xi_i} N_{i,p-1}(\xi) + \frac{\xi_{i+1+p} - \xi}{\xi_{i+1+p} - \xi_{i+1}} N_{i+1,p-1}(\xi) \quad (4)$$

The NURBS is the extension of the B-spline. The basis functions of the NURBS surface can be obtained by

$$R_{i,j}^{p,q}(\xi, \eta) = \frac{N_{i,p}(\xi)N_{j,q}(\eta)w_{i,j}}{W(\xi, \eta)} \quad (5)$$

with

$$W(\xi, \eta) = \sum_{i=1}^n \sum_{j=1}^m N_{i,p}(\xi)N_{j,q}(\eta)w_{i,j} \quad (6)$$

where $\xi \in \{\xi_0, \dots, \xi_n\}$ and $\eta \in \{\eta_0, \dots, \eta_m\}$ for two directions, $N_{i,p}(\xi)$ and $N_{j,q}(\eta)$ are the univariate B-spline basis functions of orders p and q corresponding to knot vectors in the parametric directions ξ and η . $w_{i,j}$ is the weight of control point, which decides the shape of the NURBS surface, and n and m are the numbers of basis functions in the parametric directions ξ and η . The NURBS surface with degree $p \times q$ can be defined as

$$S(\xi, \eta) = \sum_{i=1}^n \sum_{j=1}^m R_{i,j}^{p,q}(\xi, \eta) \mathbf{P}_{i,j} \quad (7)$$

where $\mathbf{P}_{i,j}$ means the control point.

3.2. Boundary integral equation (BIE)

Considering the elastic problems in the finite domain Ω enclosed by boundary Γ and neglecting body force, the BIE is defined as follows [47]:

$$c_{ij}(P)u_j(P) = \int_{\Gamma} U_{ij}^*(P, Q)t_j(Q)d\Gamma(Q) - \int_{\Gamma} T_{ij}^*(P, Q)u_j(P)d\Gamma(Q) \quad (8)$$

where $c_{ij}(P)$ ($i, j = 1, 2, 3$) depend on the boundary geometry of source points P , and Q denote the field points around boundary Γ . $U_{ij}^*(P, Q)$ and $T_{ij}^*(P, Q)$ are the fundamental solutions of displacement and traction for

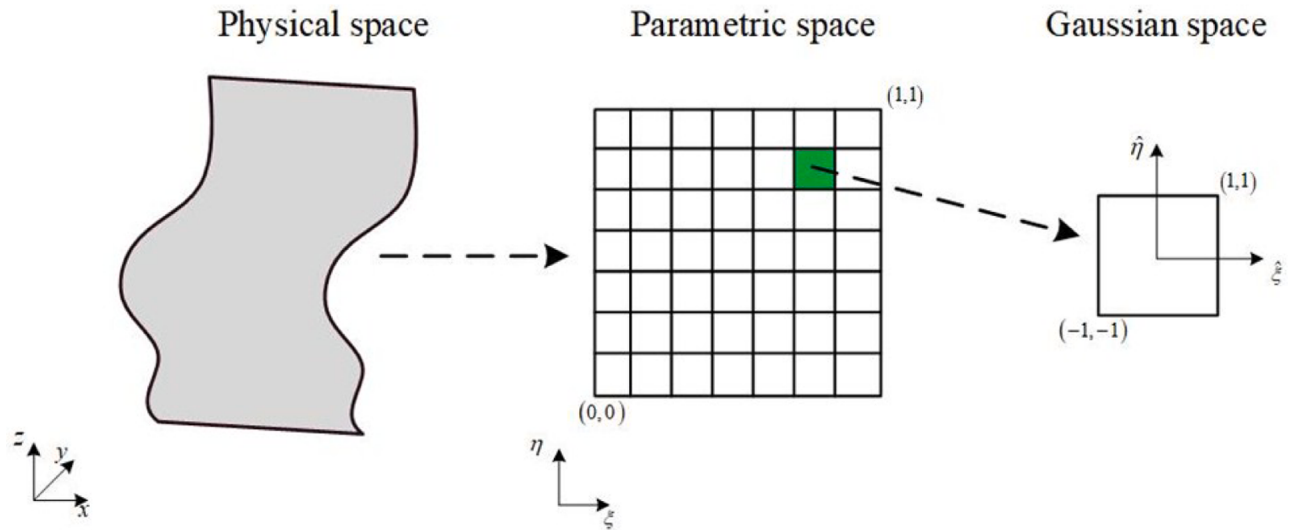


Fig. 1. The space transformations in IGABEM.

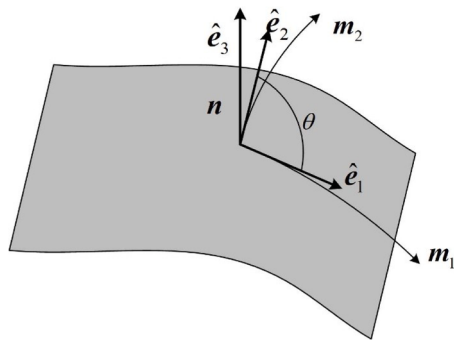


Fig. 2. Local coordinate system.

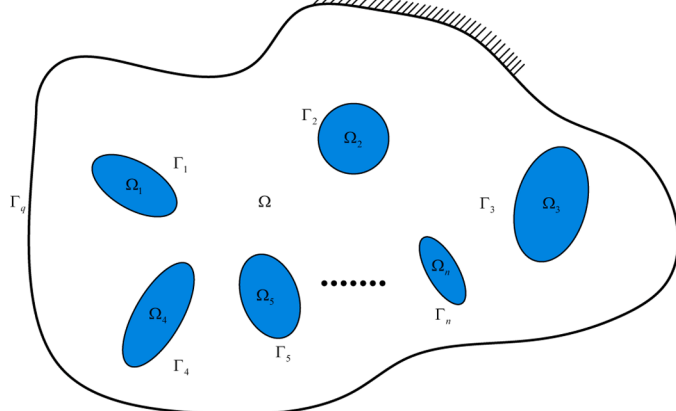


Fig. 3. The model of the elastic matrix with randomly distributed liquid inclusions.

Table 1
Polynomial orders and knot vectors.

| Geometry | Direction | Orders | Knot vectors |
|---------------------------|-----------|--------|--|
| Square/Circle/ Ellipse | ξ | 2 | $\Xi = \{0, 0, 0, 1/4, 1/4, 1/2, 1/2, 3/4, 3/4, 1, 1, 1\}$ |
| Sphere/Ellipsoid | ξ | 2 | $\Xi = \{0, 0, 0, 1/4, 1/4, 1/2, 1/2, 3/4, 3/4, 1, 1, 1\}$ |
| | η | 2 | $\Psi = \{0, 0, 0, 1/2, 1/2, 1, 1, 1\}$ |

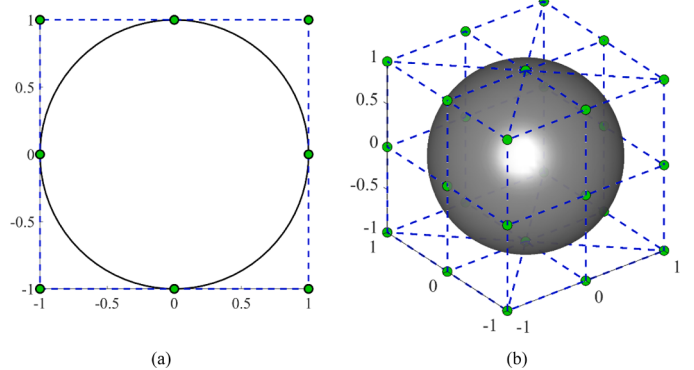


Fig. 4. Geometry and the initial control points of the liquid inclusion: (a) 2D problem; (b) 3D problem.

isotropic elastic medium, and the formulas for 3D problem are given as:

$$\begin{cases} U_{ij}^* = \frac{1}{16\pi\mu(1-\nu)r} [(3-4\nu)\delta_{ij} + r_j r_{,i}] \\ T_{ij}^* = -\frac{1}{8\pi(1-\nu)r^2} \left\{ \frac{\partial r}{\partial n} [(1-2\nu)\delta_{ij} + 3r_j r_{,i}] + (1-2\nu)(n_i r_j - n_j r_i) \right\} \end{cases} \quad (9)$$

where μ is the shear modulus, and ν is the Poisson's ratio. n_i and n_j are the components of the unit normal vector \mathbf{n} . r denotes the distance between the source point P and field point Q , and $r_{,i} = \partial r(P, Q) / \partial x_i(Q)$. For infinite domain, the BIE becomes [48]

$$c_{ij}(P)u_j(P) = \int_{\Gamma} U_{ij}^*(P, Q)t_j(Q)d\Gamma(Q) - \int_{\Gamma} T_{ij}^*(P, Q)u_j(P)d\Gamma(Q) + u_0 \quad (10)$$

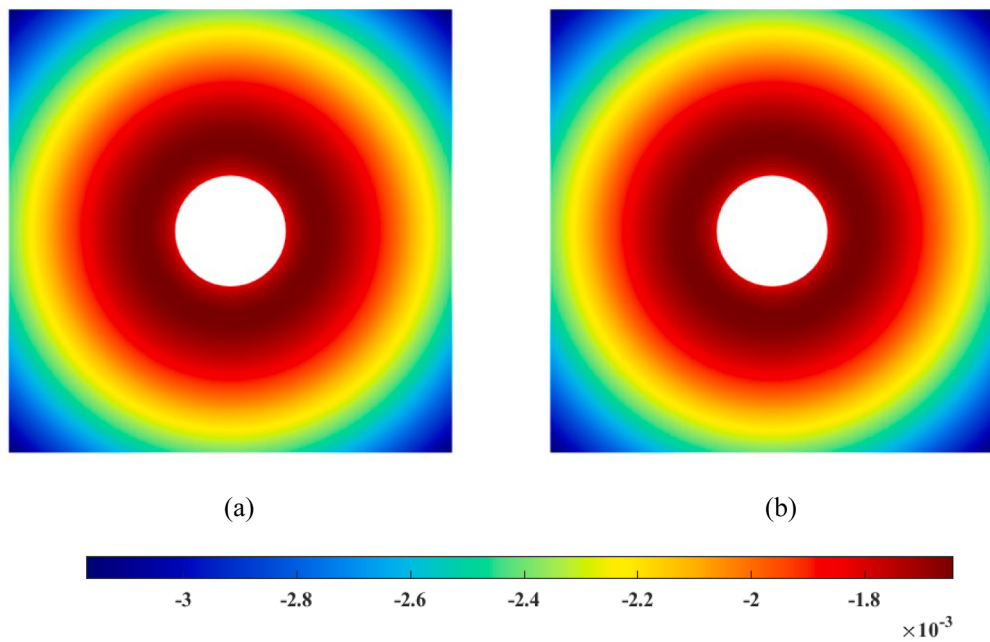


Fig. 5. Radial displacement computed by analytical method and IGABEM: (a) Numerical results; (b) Analytical solution.

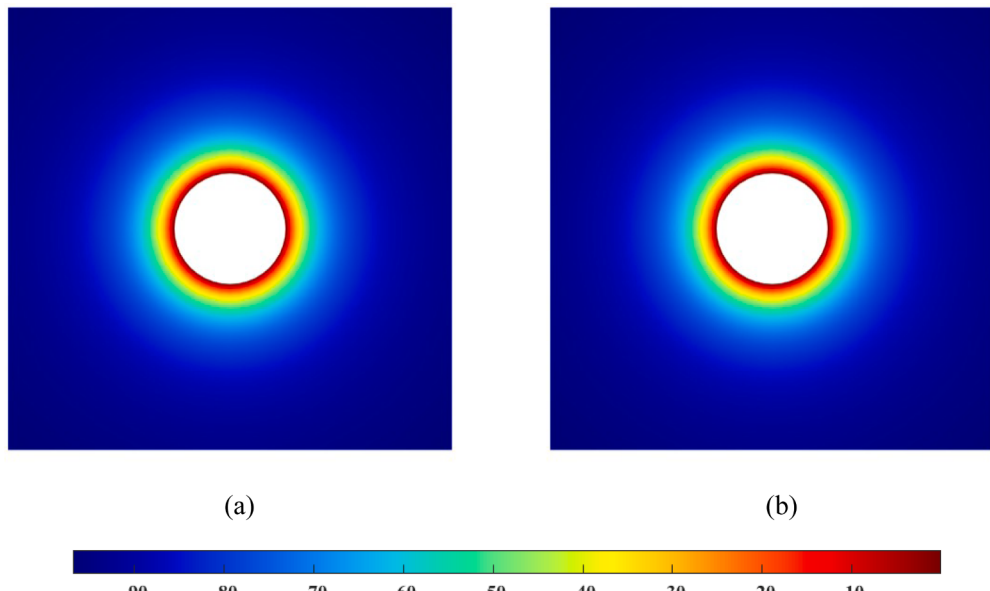


Fig. 6. Radial stress computed by analytical method and IGABEM: (a) Numerical results; (b) Analytical solution.

Table 2
Pressure of liquid inclusion.

| K/E | Analytical solution [17] | IGABEM | Errors |
|--------------------|--------------------------|---------|------------|
| 1×10^{-2} | 3.54776 | 3.54776 | 6.67E – 07 |
| 1×10^{-1} | 28.8889 | 28.8889 | 4.01E – 06 |
| 1×10^0 | 101.111 | 101.110 | 1.35E – 05 |
| 1×10^1 | 134.815 | 134.812 | 1.80E – 05 |

Table 3
Radial displacement at $r = 2$.

| K/E | Analytical solution [17] | IGABEM | Errors |
|--------------------|--------------------------|----------------|------------|
| 1×10^{-2} | – 1.6669E – 03 | – 1.6669E – 03 | 2.18E – 07 |
| 1×10^{-1} | – 1.5022E – 03 | – 1.5022E – 03 | 6.72E – 08 |
| 1×10^0 | – 1.0328E – 03 | – 1.0328E – 03 | 7.22E – 06 |
| 1×10^1 | – 8.1370E – 04 | – 8.1372E – 04 | 1.71E – 05 |

Table 4Radial stress at $r = 2$.

| | Analytical solution [17] | IGABEM | Errors |
|--------------------|--------------------------|-----------|------------|
| 1×10^{-2} | – 75.8869 | – 75.8869 | 2.83E – 08 |
| 1×10^{-1} | – 82.2222 | – 82.2220 | 2.51E – 06 |
| 1×10^0 | – 100.278 | – 100.277 | 1.03E – 05 |
| 1×10^1 | – 108.704 | – 108.702 | 1.41E – 05 |

Table 5

Pressure of the liquid inclusion.

| K/E | Analytical solution | IGABEM | Errors |
|--------------------|---------------------|---------------|------------|
| 1×10^{-2} | 3.08975E – 02 | 3.08975E – 02 | 2.83E – 07 |
| 1×10^{-1} | 2.63598E – 01 | 2.63598E – 01 | 5.73E – 07 |
| 1×10^0 | 1.06780 | 1.06780 | 1.57E – 06 |
| 1×10^1 | 1.59659 | 1.53659 | 2.16E – 06 |

Table 6Radial displacement at $r = 2$.

| K/E | Analytical solution | IGABEM | Errors |
|--------------------|---------------------|-----------------|------------|
| 1×10^{-2} | – 9.57479E – 04 | – 9.57479E – 04 | 2.02E – 08 |
| 1×10^{-1} | – 9.19665E – 04 | – 9.19665E – 04 | 1.38E – 08 |
| 1×10^0 | – 7.88983E – 04 | – 7.88983E – 04 | 2.27E – 07 |
| 1×10^1 | – 7.12804E – 04 | – 7.12804E – 04 | 5.77E – 07 |

Table 7Radial stress at $r = 2$.

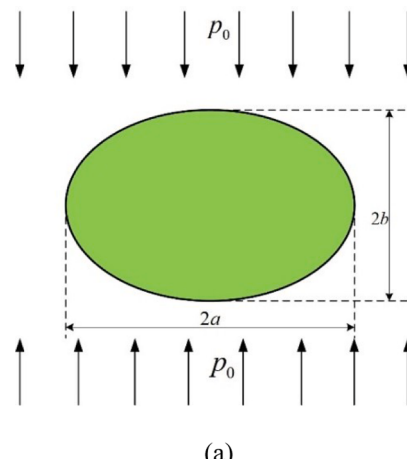
| K/E | Analytical solution | IGABEM | Errors |
|--------------------|---------------------|-----------------|------------|
| 1×10^{-2} | – 8.78862E – 01 | – 8.78862E – 01 | 2.64E – 08 |
| 1×10^{-1} | – 9.07950E – 01 | – 9.07950E – 01 | 3.47E – 08 |
| 1×10^0 | – 1.00847 | – 1.00847 | 6.89E – 08 |
| 1×10^1 | – 1.06707 | – 1.06707 | 2.07E – 07 |

where u_0 denotes the displacements at the collocation point under remote load.

3.3. Implementation of IGA

In conventional BEM analysis, the boundary is usually discretized by polynomial functions with the geometric discretization errors. But this is not the case in the IGA process. In the following part, we apply the IGA to the BEM and show the framework of IGABEM.

Using NURBS approximation, the displacement and traction of



element e can be described by

$$\begin{cases} u_i = \sum_{j=1}^{p+1} \sum_{s=1}^{q+1} R_{j,s}^e(\xi, \eta) d_{j,s}^e \\ q_i = \sum_{j=1}^{p+1} \sum_{s=1}^{q+1} R_{j,s}^e(\xi, \eta) t_{j,s}^e \end{cases} \quad (11)$$

where $R_{j,s}^e$ are the NURBS basis functions, which are nonzero in the element e . $d_{j,s}^e$ and $t_{j,s}^e$ are the displacement and traction coefficients of the element e , which are not the real displacement and traction located at the boundary. Because the NURBS approximation is local supported by the control points, while the control points are usually not at the boundary. The transformations between them can be shown as:

$$\begin{cases} \mathbf{u} = \mathbf{T}_u \mathbf{d} \\ \mathbf{q} = \mathbf{T}_t \mathbf{t} \end{cases} \quad (12)$$

where \mathbf{T}_u and \mathbf{T}_t are the displacement and traction transformation matrix related to the basis functions, respectively.

For convenience, we change Eq. (11) to the common representation as

$$\begin{cases} u_i = \sum_{j=1}^{(p+1) \times (q+1)} R_j d_j \\ q_i = \sum_{j=1}^{(p+1) \times (q+1)} R_j t_j \end{cases} \quad (13)$$

where $R_j \equiv R_{j,s}^e$, $d_j \equiv d_{j,s}^e$ and $t_j \equiv t_{j,s}^e$, which are just rearranged in a row or a column. Substituting Eq. (13) into Eq. (8), we can get

$$c_{ij}(P) \sum_{k=1}^{(p+1) \times (q+1)} R_k d_k = \sum_{l=1}^{NE} \int_{\xi_s}^{\xi_{s+1}} \int_{\eta_l}^{\eta_{l+1}} U_{ij}^*(P, Q) \sum_{k=1}^{(p+1) \times (q+1)} R_k t_k J_1(\xi, \eta) d\xi d\eta - \sum_{l=1}^{NE} \int_{\xi_s}^{\xi_{s+1}} \int_{\eta_l}^{\eta_{l+1}} T_{ij}^*(P, Q) \sum_{k=1}^{(p+1) \times (q+1)} R_k d_k J_1(\xi, \eta) d\xi d\eta \quad (14)$$

where NE is the number of the boundary element.

In the implementation of IGABEM, the global coordinates in physical space need to be transformed to the Gaussian space for the numerical computation. The process is shown in Fig. 1. Therefore, the Jacobian $J_1(\xi, \eta)$ in Eq. (14) is the result of the transformation from physical space to parametric space $(\xi, \eta) \in [\xi_s, \xi_{s+1}] \times [\eta_l, \eta_{l+1}]$, which is given as

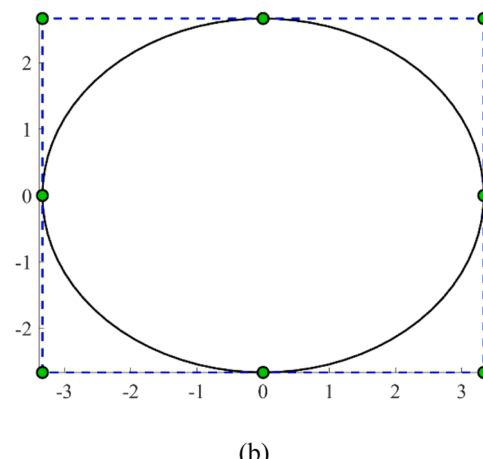


Fig. 7. An elliptical liquid inclusion in the infinite plane: (a) Under remote uniaxial load p_0 ; (b) Geometry and the initial control points of the liquid inclusion.

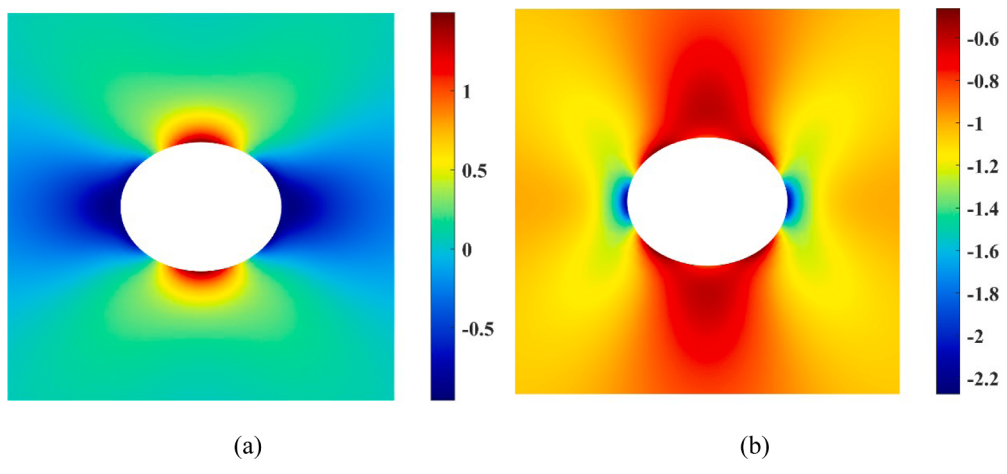


Fig. 8. Stress field around the liquid inclusion with the shape parameter $R = 3$ and $K' = 1$: (a) Stress field in x -direction; (b) Stress field in y -direction.

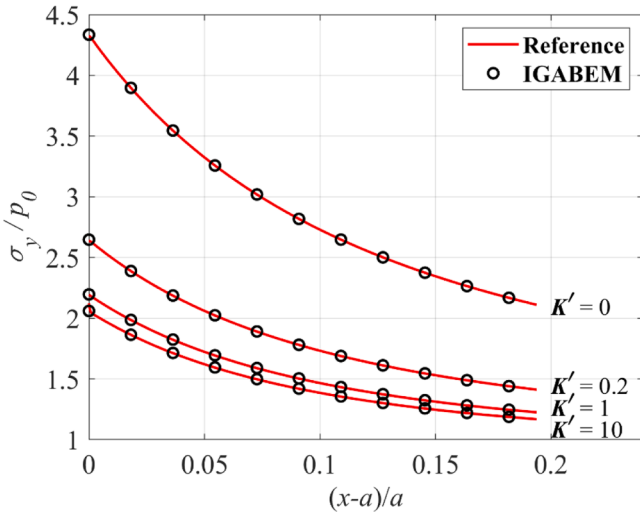


Fig. 9. Stress along the x -axis with the shape parameter $R=2$.

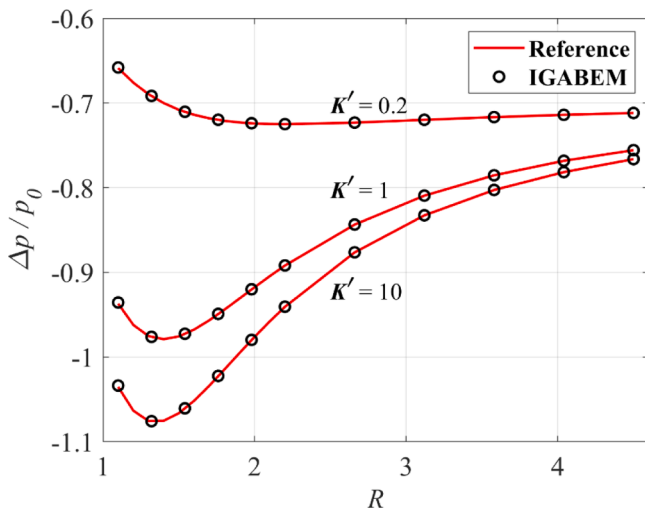


Fig. 10. Pressure variation under different shape parameters.

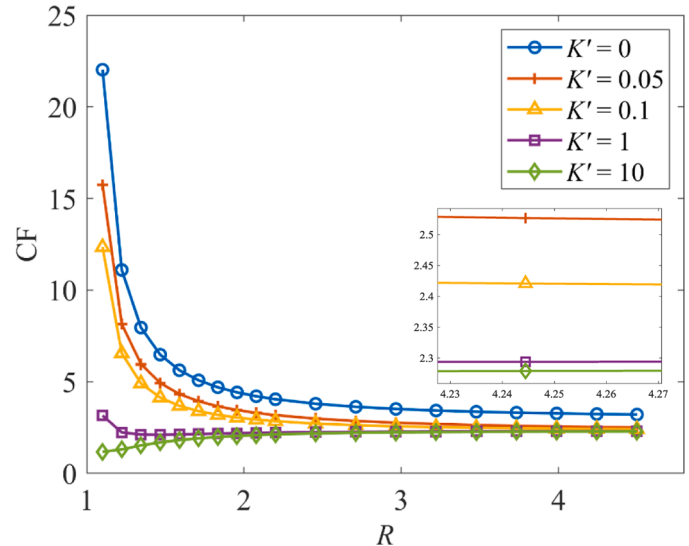


Fig. 11. Stress concentration factor under different shape parameters and different values of K' .

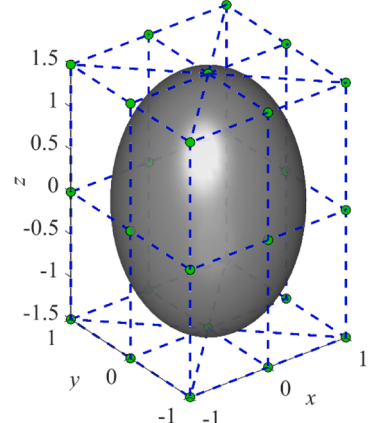


Fig. 12. The initial control points of the liquid inclusion when the aspect ratio is 1:1:1.5.

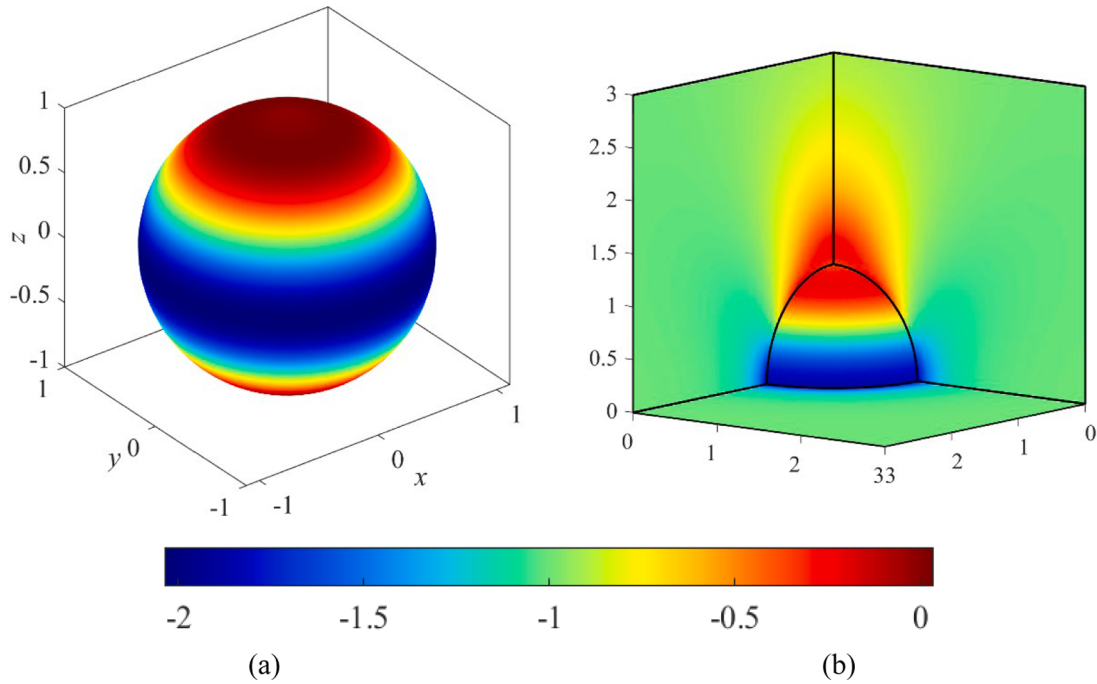


Fig. 13. Stress field around the liquid inclusion: (a) Stress field at the interface; (b) Stress field of the matrix around the liquid inclusion.

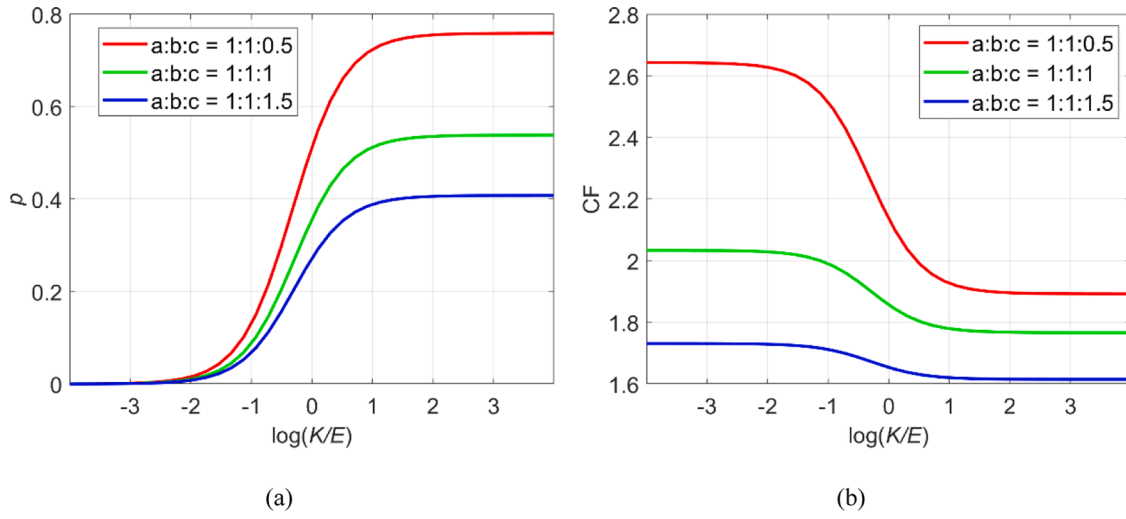


Fig. 14. The effect of the bulk modulus under different aspect ratios: (a) The inner pressure under load; (b) The stress concentration factor.

$$J_1(\xi, \eta) = \begin{vmatrix} \mathbf{i} & \mathbf{j} & \mathbf{k} \\ \frac{\partial x}{\partial \xi} & \frac{\partial y}{\partial \xi} & \frac{\partial z}{\partial \xi} \\ \frac{\partial x}{\partial \eta} & \frac{\partial y}{\partial \eta} & \frac{\partial z}{\partial \eta} \end{vmatrix} \quad (15)$$

$$= \sqrt{\left(\frac{\partial y}{\partial \xi} \frac{\partial z}{\partial \eta} - \frac{\partial z}{\partial \xi} \frac{\partial y}{\partial \eta}\right)^2 + \left(\frac{\partial z}{\partial \xi} \frac{\partial x}{\partial \eta} - \frac{\partial x}{\partial \xi} \frac{\partial z}{\partial \eta}\right)^2 + \left(\frac{\partial x}{\partial \xi} \frac{\partial y}{\partial \eta} - \frac{\partial y}{\partial \xi} \frac{\partial x}{\partial \eta}\right)^2}$$

The Jacobian in another transformation from parametric space $(\xi, \eta) \in [\xi_s, \xi_{s+1}] \times [\eta_l, \eta_{l+1}]$ to Gaussian space $(\hat{\xi}, \hat{\eta}) \in [-1, 1] \times [-1, 1]$ is given by

$$J_2(\hat{\xi}, \hat{\eta}) = \frac{(\xi_{s+1} - \xi_s)(\eta_{l+1} - \eta_l)}{4} \quad (16)$$

Applying the transformations to Eq. (14) gives us the following

expression:

$$c_{ij}(P) \sum_{k=1}^{(p+1) \times (q+1)} R_k d_k = \sum_{l=1}^{NE} \int_{-1}^1 \int_{-1}^1 U_{ij}^*(P, Q) \sum_{k=1}^{(p+1) \times (q+1)} R_k t_k J_1(\hat{\xi}, \hat{\eta}) d\hat{\xi} d\hat{\eta} - \sum_{l=1}^{NE} \int_{-1}^1 \int_{-1}^1 T_{ij}^*(P, Q) \sum_{k=1}^{(p+1) \times (q+1)} R_k d_k J_1(\hat{\xi}, \hat{\eta}) d\hat{\xi} d\hat{\eta} \quad (17)$$

In addition, we need to obtain the position of collocation points, which are located at the geometric boundary and related to the control points. We usually get the collocation point in parametric space by Greville abscissae definition [49], i.e.

$$\xi'_i = \frac{\xi_{i+1} + \xi_{i+2} + \dots + \xi_{i+p}}{p} \quad i = 1, 2, \dots, n \quad (18)$$

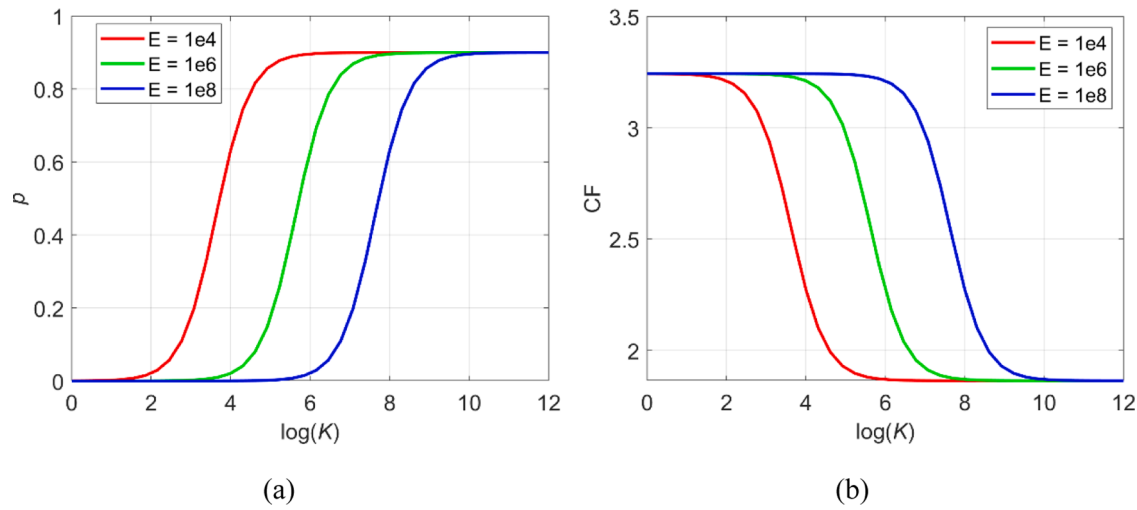


Fig. 15. The relationship between Young's modulus of the matrix and bulk modulus of the liquid inclusion: (a) The inner pressure; (b) The stress concentration factor.

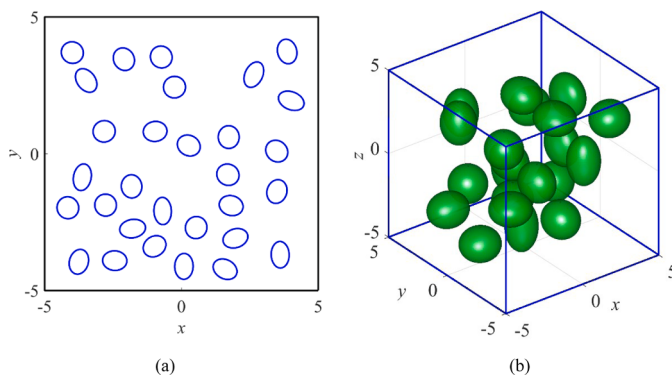


Fig. 16. Randomly distributed liquid inclusions: (a) 2D plane; (b) 3D space.

Table 8
The polynomial orders and knot vectors of cube.

| Geometry | Directions | Orders | Knot vectors |
|----------|------------|--------|--|
| Cube | ξ | 2 | $\Xi = \{0, 0, 0, 1/4, 1/4, 1/2, 1/2, 3/4, 3/4, 1, 1, 1\}$ |
| | η | 2 | $\Psi = \{0, 0, 0, 1/3, 1/3, 2/3, 2/3, 3, 1, 1, 1\}$ |

$$\eta'_j = \frac{\eta_{j+1} + \eta_{j+2} + \dots + \eta_{j+q}}{q}, j = 1, 2, \dots, m \quad (19)$$

where n and m are the number of control points in ξ and η directions. p and q are the orders of the curve in the ξ and η directions, respectively.

Combining the BIEs at all collocation points, we can get the system of equations for the elastic problem as:

$$\mathbf{Hd} = \mathbf{Gt} \quad (20)$$

By moving unknown values in Eq. (20) to the left and known values to the right, we can get

$$\mathbf{Ax} = \mathbf{b} \quad (21)$$

where \mathbf{x} contains all unknown components of displacement and traction. By solving Eq. (21), we can get all values of displacement and traction on the boundary.

In numerical implementation, we need to deal with the singular integrals in the IGABEM. For 2D problems, the SST method [38] has been

used for strongly singular integrals, and the Tolls transformation [39] is used to deal with weakly singular integrals. For 3D problems, we adopt the power series expansion method [40,41] to solve both the strongly and weakly singular integrals.

3.4. Postprocessing

After solving Eq. (21), we can compute displacement and stress at internal point. The displacement expression at internal point is given as [50]

$$u_j^I(P) = \int_{\Gamma} U_{ij}^*(P, Q) t_j(Q) d\Gamma(Q) - \int_{\Gamma} T_{ij}^*(P, Q) u_j(P) d\Gamma(Q) \quad (22)$$

where P denote the inner source points, and Q denote the field points on the boundary. Similarly, we have the stress expression at the internal point [50]

$$\sigma_{ij}^I = \int_{\Gamma} D_{kij}(P, Q) t_k(Q) d\Gamma(Q) - \int_{\Gamma} S_{kij}(P, Q) u_k(P) d\Gamma(Q) \quad (23)$$

where D_{kij} and S_{kij} in 3D problem are listed as follows [50]:

$$\left\{ \begin{array}{l} D_{kij} = \frac{1}{8\pi(1-\nu)r^2} [(1-2\nu)(\delta_{ik}r_j + \delta_{jk}r_i - \delta_{ij}r_k) + 3r_ir_jr_k] \\ S_{kij} = \frac{\mu}{4\pi(1-\nu)r^3} \left\{ 3\frac{\partial r}{\partial n} [(1-2\nu)\delta_{ij}r_k + \nu(r_j\delta_{ik} + r_i\delta_{jk}) - 5r_ir_jr_k] \right\} \\ \quad + \frac{\mu}{4\pi(1-\nu)r^3} \{ 3\nu(n_ir_jr_k + n_jr_ir_k) \} \\ \quad + \frac{\mu}{4\pi(1-\nu)r^3} \{ (1-2\nu)(3n_kr_ir_j + n_j\delta_{ik} + n_i\delta_{jk}) - (1-4\nu)n_k\delta_{ij} \} \end{array} \right. \quad (24)$$

The stress on the boundary can also be computed by Eq. (23), but the hypersingular integral needs to be solved. In order to avoid the calculation of the hypersingular integral, we solve the stress on the boundary based on the constitutive equation in the local coordinate system [50], which is a simple and effective method. For 3D problem, the vector in local coordinate system can be described as

$$\hat{\mathbf{r}} = \hat{x}\hat{\mathbf{e}}_1 + \hat{y}\hat{\mathbf{e}}_2 + \hat{z}\hat{\mathbf{e}}_3 \quad (25)$$

where $\hat{\mathbf{e}}_i (i=1, 2, 3)$ is the unit vector along the i -th axis in local coordinate system, which can be defined as

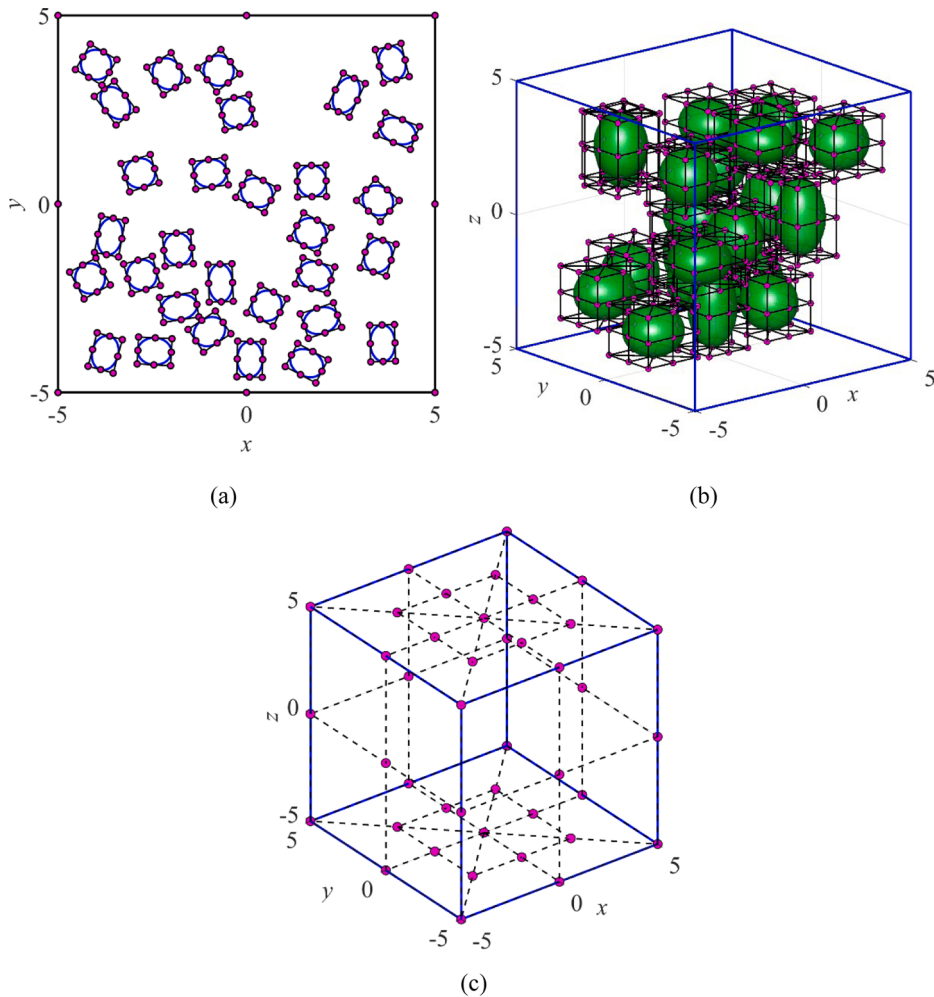


Fig. 17. The initial control points of the randomly distributed liquid inclusions: (a) The control points of 2D problem; (b) The control points of 3D liquid inclusions; (c) The control points of 3D outer boundary.

$$\hat{\mathbf{e}}_1 = \frac{\mathbf{m}_1}{|\mathbf{m}_1|}, \hat{\mathbf{e}}_3 = \frac{\mathbf{n}}{|\mathbf{n}|}, \hat{\mathbf{e}}_2 = \hat{\mathbf{e}}_1 \times \hat{\mathbf{e}}_3 \quad (26)$$

where \mathbf{m}_1 , \mathbf{m}_2 and \mathbf{n} are shown in Fig. 2 and their expressions are given as

$$\mathbf{m}_1 = \frac{\partial \mathbf{r}}{\partial \xi_1}, \mathbf{m}_2 = \frac{\partial \mathbf{r}}{\partial \xi_2}, \mathbf{n} = \mathbf{m}_1 \times \mathbf{m}_2 \quad (27)$$

The transformation matrix can be written as:

$$A = \begin{bmatrix} \hat{\mathbf{e}}_1 \\ \hat{\mathbf{e}}_2 \\ \hat{\mathbf{e}}_3 \end{bmatrix} \quad (28)$$

Besides, we need the following formulas:

$$\frac{\partial \xi_1}{\partial \hat{x}_1} = \frac{1}{|\mathbf{m}_1|}, \frac{\partial \xi_1}{\partial \hat{x}_2} = \frac{-\cos\theta}{|\mathbf{m}_1|\sin\theta} \quad (29)$$

$$\frac{\partial \xi_2}{\partial \hat{x}_1} = 0, \frac{\partial \xi_2}{\partial \hat{x}_2} = \frac{1}{|\mathbf{m}_2|}\sin\theta \quad (30)$$

where \hat{x}_1 , \hat{x}_2 and \hat{x}_3 represent the local coordinate system. Then, we can get the local strain in $\hat{\mathbf{e}}_1 - \hat{\mathbf{e}}_2$ plane as

$$\hat{\varepsilon}_{ij} = \frac{\partial \hat{u}_i}{\partial \hat{x}_j} = \frac{\partial \hat{u}_i}{\partial \xi_k} \frac{\partial \xi_k}{\partial \hat{x}_j} (i, j, k = 1, 2) \quad (31)$$

and

$$\frac{\partial \hat{u}_i}{\partial \xi_k} = A_{ik} \frac{\partial u_l}{\partial \xi_k} (k = 1, 2 \text{ and } i, l = 1, 2, 3) \quad (32)$$

Therefore, the stress at local coordinate system can be obtained as

$$\begin{cases} \hat{\sigma}_{11} = \frac{E}{1-\nu^2} (\hat{\varepsilon}_{11} + \nu \hat{\varepsilon}_{22}) + \frac{\nu}{1-\nu} \hat{t}_1 \\ \hat{\sigma}_{12} = \frac{E}{1+\nu} \hat{\varepsilon}_{12} \\ \hat{\sigma}_{22} = \frac{E}{1-\nu^2} (\hat{\varepsilon}_{22} + \nu \hat{\varepsilon}_{11}) + \frac{\nu}{1-\nu} \hat{t}_3 \end{cases} \quad (33)$$

and

$$\hat{\sigma}_{33} = \hat{t}_3, \hat{\sigma}_{23} = \hat{t}_2, \hat{\sigma}_{13} = \hat{t}_1 \quad (34)$$

Finally, we get the stress at global coordinate system by

$$\sigma_{ij} = A_{ki} A_{nj} \hat{\sigma}_{kn} \quad (35)$$

3.5. Liquid inclusion problems by IGABEM

In this subsection, we use IGABEM to solve the problems of randomly distributed liquid inclusions embedded in the matrix. In order to show the solution process, we discuss the common situation in 2D problems.

As shown in Fig. 3, Γ_u and Γ_q are the prescribed displacement and traction boundaries of elastic domain Ω . And there are numerous randomly distributed liquid inclusions $\Omega_1, \dots, \Omega_n$ with the interfaces $\Gamma_1, \dots,$

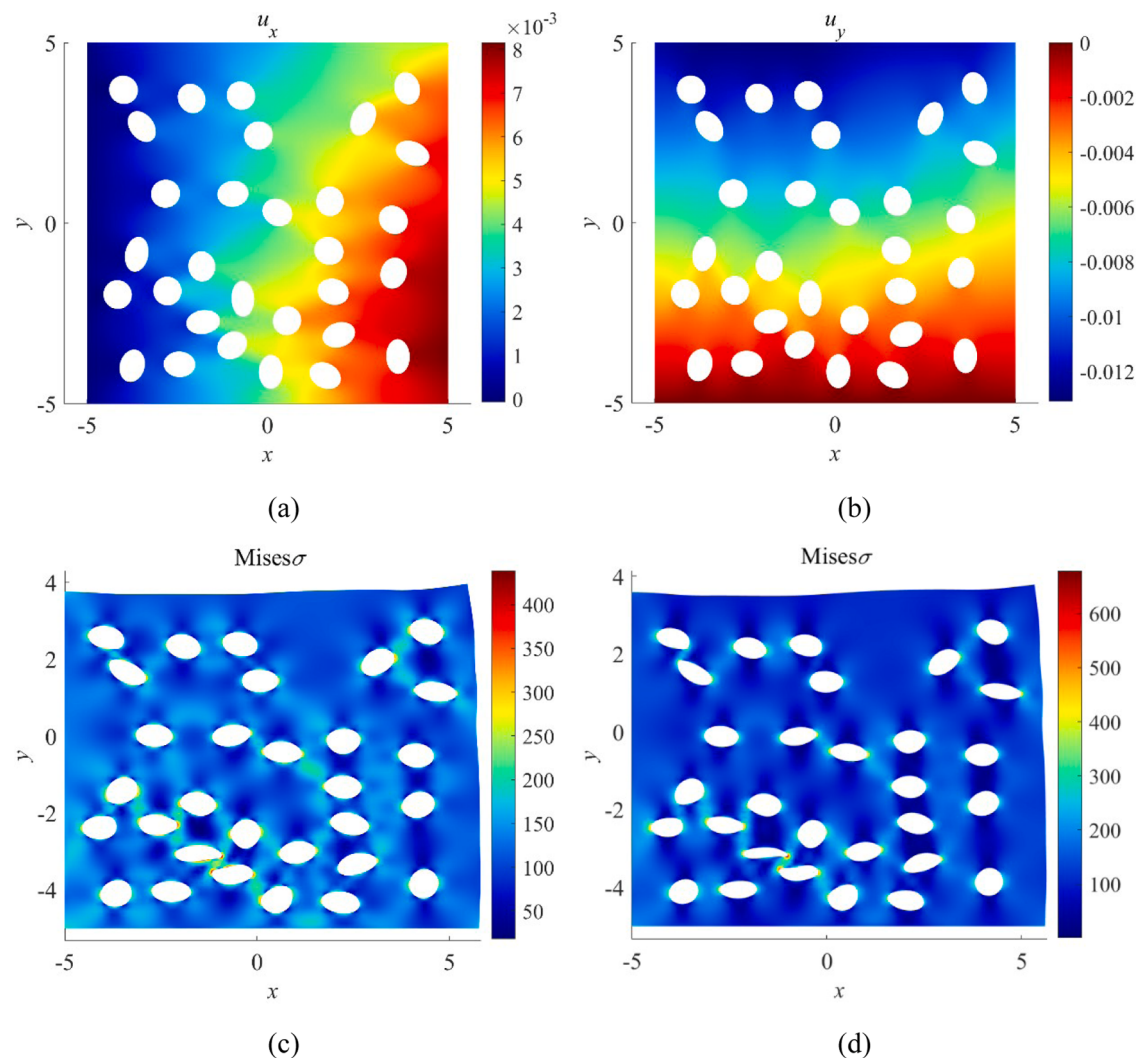


Fig. 18. The displacement and stress fields of the randomly distributed liquid inclusions for 2D problem: (a) Displacement in x -direction; (b) Displacement in y -direction; (c) Mises stress for liquid inclusions; (d) Mises stress for holes.

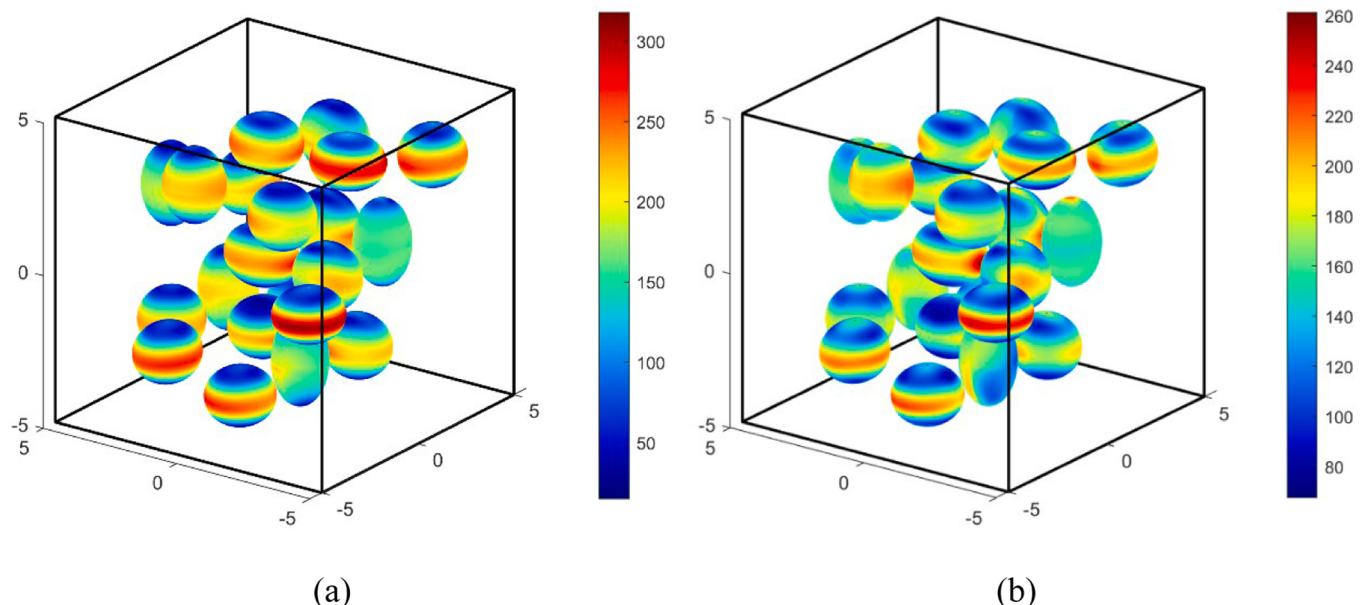


Fig. 19. The stress filed of the randomly distributed liquid inclusions for 3D problem: (a) Mises stress for holes; (b) Mises stress for liquid inclusions.

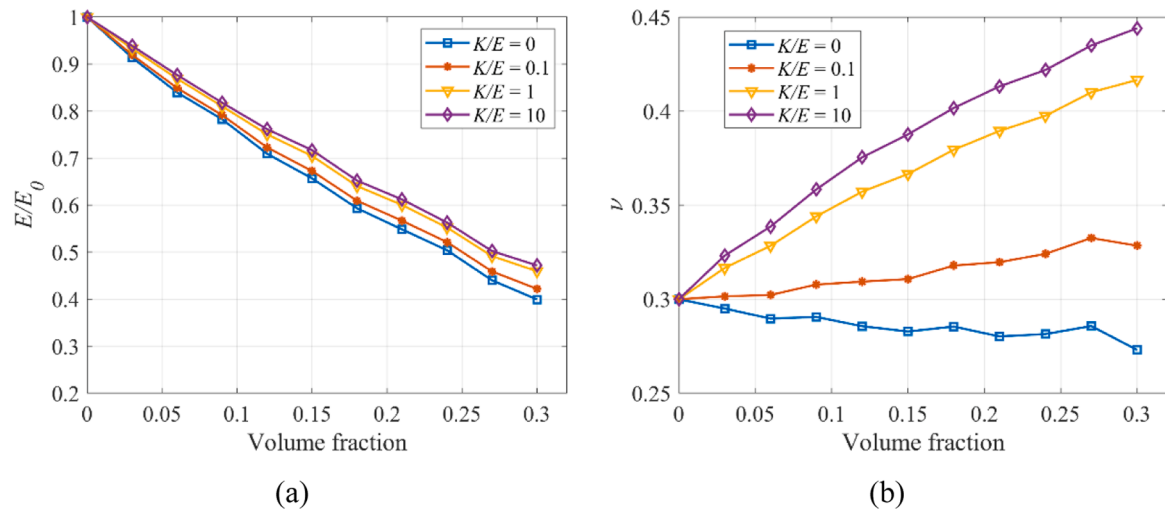


Fig. 20. Effective elastic modulus and effective Poisson's ratio for 2D problem: (a) Effective Young's modulus; (b) Effective Poisson's ratio.

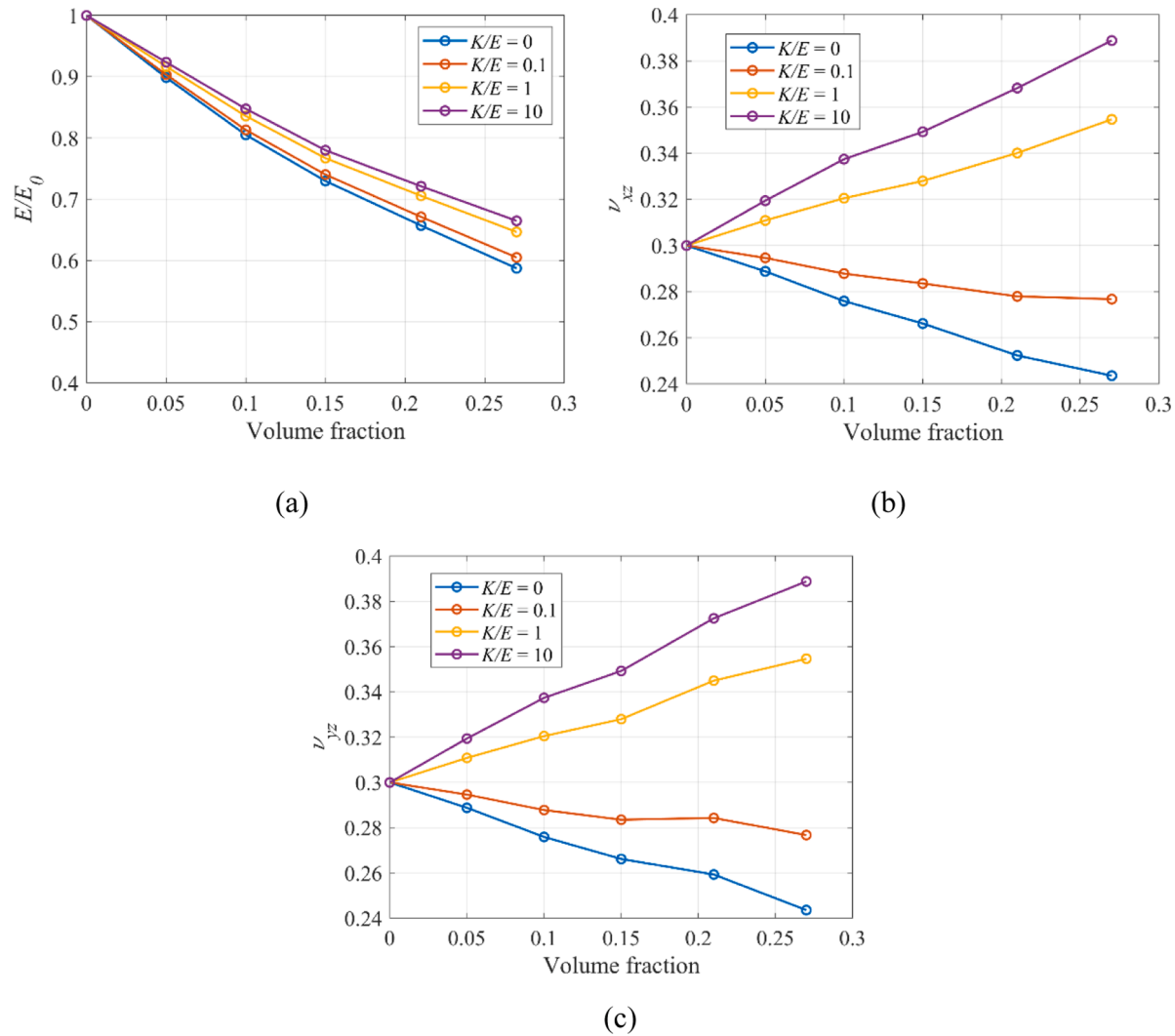


Fig. 21. Effective elastic modulus and effective Poisson's ratio for 3D problem: (a) Effective Young's modulus; (b) x-z components of effective Poisson's ratio; (c) y-z components of effective Poisson's ratio.

... Γ_n . Firstly, the IGABEM equation of the elastic matrix is obtained according to Eq. (20):

$$\begin{bmatrix} \mathbf{h}_{00} & \mathbf{h}_{01} & \cdots & \mathbf{h}_{0n} \\ \mathbf{h}_{10} & \mathbf{h}_{11} & \cdots & \mathbf{h}_{1n} \\ \cdots & \cdots & \cdots & \cdots \\ \mathbf{h}_{n0} & \mathbf{h}_{n1} & \cdots & \mathbf{h}_{nn} \end{bmatrix} \begin{Bmatrix} \mathbf{d}_0 \\ \mathbf{d}_1 \\ \cdots \\ \mathbf{d}_n \end{Bmatrix} = \begin{bmatrix} \mathbf{g}_{00} & \mathbf{g}_{01} & \cdots & \mathbf{g}_{0n} \\ \mathbf{g}_{10} & \mathbf{g}_{11} & \cdots & \mathbf{g}_{1n} \\ \cdots & \cdots & \cdots & \cdots \\ \mathbf{g}_{n0} & \mathbf{g}_{n1} & \cdots & \mathbf{g}_{nn} \end{bmatrix} \begin{Bmatrix} \mathbf{t}_0 \\ \mathbf{t}_1 \\ \cdots \\ \mathbf{t}_n \end{Bmatrix} \quad (36)$$

where $\mathbf{d}_0, \mathbf{d}_1, \dots, \mathbf{d}_n$ and $\mathbf{t}_0, \mathbf{t}_1, \dots, \mathbf{t}_n$ are the displacement and traction coefficient vectors. Subscript 0 denotes quantities on the outer boundary, and subscripts 1-n denote quantities on the interfaces 1-n. Such members as \mathbf{h}_{11} and \mathbf{g}_{11} in Eq. (36) are sub-matrices related to the displacement and traction coefficients. Some components in $\mathbf{d}_0, \mathbf{t}_0$ and all the values of $\mathbf{d}_1, \dots, \mathbf{d}_n, \mathbf{t}_1, \dots, \mathbf{t}_n$ are unknown. Thus, the Eq. (36) cannot be solved directly.

At the liquid-matrix interface, the interface condition is shown in Eq. (2), where the relationship between traction and pressure p is given. The pressure p can be obtained by Eq. (1), where the area variation ΔV under small deformation assumption is given as:

$$\Delta V = \oint u_n ds \quad (37)$$

where

$$\mathbf{u}_n = \mathbf{n} \cdot \mathbf{u} = n_x u_x + n_y u_y \quad (38)$$

\mathbf{n} and \mathbf{u} are the outer unit normal and displacement vectors on the boundary of liquid inclusion, respectively. By Eqs. (13) and (38), and discretizing the liquid-matrix interface, Eq. (37) becomes

$$\Delta V = \sum_{I=1}^{NE} \int_{\xi_I}^{\xi_{I+1}} \int_{\eta_I}^{\eta_{I+1}} \mathbf{n} \mathbf{N}_k \mathbf{d}_k J d\xi d\eta \quad (39)$$

where NE are the total number of the element, and

$$\mathbf{N}_k = \begin{bmatrix} R_k & 0 \\ 0 & R_k \end{bmatrix} \quad (40)$$

$$\mathbf{d}_k = \begin{bmatrix} d_{kx} \\ d_{ky} \end{bmatrix} \quad (41)$$

We can simplify Eq. (39) as:

$$\Delta V = \mathbf{M} \mathbf{d} \quad (42)$$

where \mathbf{d} contains the displacement coefficients and it is a column vector. \mathbf{M} is a row vector and it is expressed as:

$$\mathbf{M} = \sum_{I=1}^{NE} \int_{\xi_I}^{\xi_{I+1}} \int_{\eta_I}^{\eta_{I+1}} \mathbf{n} \mathbf{N}_k J d\xi d\eta \quad (43)$$

From Eq. (42), we get the relationship between the area variation and displacement coefficients. According to Eqs. (1), (2) and (42), we can obtain the traction shown as

$$\bar{\mathbf{q}}^M = \begin{bmatrix} q_x \\ q_y \end{bmatrix} = \bar{\mathbf{n}}^M = \bar{\mathbf{n}}^M \cdot \frac{K}{V} \mathbf{M} \mathbf{d}^{in} \quad (44)$$

where $\bar{\mathbf{q}}^M$ is the traction vector related to $\bar{\mathbf{n}}^M$ at a single collocation point, and \mathbf{d}^{in} is the displacement coefficients vector at all the collocation points. The superscript M stands for the elastic matrix and the superscript I stands for the liquid inclusion. In addition, we should notice that $\bar{\mathbf{n}}^M$ is the outer unit normal of the matrix boundary, which is not the same as \mathbf{n} in Eq. (39).

Assembling Eq. (44) at all the collocation points, we can get

$$\mathbf{q}^M = \frac{K}{V} \bar{\mathbf{n}}^M \mathbf{M} \mathbf{d}^{in} \quad (45)$$

in which, \mathbf{q}^M is the traction vector of all the collocation points, and $\bar{\mathbf{n}}^M$ is

a column vector formed by outer unit normal at collocation points. The displacement and traction at the liquid-matrix interface satisfy Eq. (46).

$$\begin{cases} \mathbf{u}^M = \mathbf{u}^{in} \\ \mathbf{q}^M = -\mathbf{q}^{in} \end{cases} \quad (46)$$

Substituting Eqs. (12) and (46) to Eq. (45), we can obtain the relationship between traction coefficients and displacement coefficients as follows:

$$\mathbf{T}_t \mathbf{t}^M = \frac{K}{V} \bar{\mathbf{n}}^M \mathbf{M} \mathbf{d}^M \quad (47)$$

or

$$\begin{cases} \mathbf{t}^M = \mathbf{D} \mathbf{d}^M \\ \mathbf{D} = \frac{K}{V} \mathbf{T}_t^{-1} \bar{\mathbf{n}}^M \mathbf{M} \end{cases} \quad (48)$$

Then applying Eq. (48) to Eq. (36), we will obtain

$$\mathbf{t}_n = \mathbf{D}_n \mathbf{d}_n \quad (49)$$

By rearranging the position of the submatrix, we can get the solution equation as

$$\begin{bmatrix} \mathbf{a}_{00} & \mathbf{h}_{01} - \mathbf{g}_{01} \mathbf{D}_1 & \cdots & \mathbf{h}_{0n} - \mathbf{g}_{0n} \mathbf{D}_n \\ \mathbf{a}_{10} & \mathbf{h}_{11} - \mathbf{g}_{11} \mathbf{D}_1 & \cdots & \mathbf{h}_{1n} - \mathbf{g}_{1n} \mathbf{D}_n \\ \cdots & \cdots & \cdots & \cdots \\ \mathbf{a}_{n0} & \mathbf{h}_{n1} - \mathbf{g}_{n1} \mathbf{D}_1 & \cdots & \mathbf{h}_{nn} - \mathbf{g}_{nn} \mathbf{D}_n \end{bmatrix} \begin{Bmatrix} \mathbf{x} \\ \mathbf{d}_1 \\ \cdots \\ \mathbf{d}_n \end{Bmatrix} = \{\mathbf{b}\} \quad (50)$$

where \mathbf{x} contains the unknown displacement and traction coefficients of \mathbf{d}_0 and \mathbf{t}_0 . And $\{\mathbf{b}\}$ is the column vector obtained by the prescribed values of \mathbf{d}_0 and \mathbf{t}_0 . By solving Eq. (50), we can get all the unknown values. The liquid pressure can be obtained by Eq. (1). In addition, if needed, the stresses on the boundary and at internal points can be calculated by using the method in Section 3.4.

4. Numerical examples

In this section, we first verify the accuracy of the IGABEM for 2D and 3D liquid inclusion problems in part 4.1. Then the elastic field of a single liquid inclusion under remote uniaxial load is studied in 4.2. Finally, the effective mechanical properties of the matrix with randomly distributed liquid inclusions are computed by using the representative volume element (RVE) in 4.3.

4.1. Verification for IGABEM

To verify the accuracy of IGABEM, the 2D infinite elastic matrix containing a circular liquid inclusion under the remote biaxial pressure p_0 is studied. The analytical solutions [17] for the pressure p of the liquid, the radial stress and displacement are given as

$$p = \frac{4K(1-\nu^2)}{2K(1+\nu)+E} p_0 \quad (51)$$

$$\sigma_r = -\frac{a^2}{r^2} p - \left(1 - \frac{a^2}{r^2} p_0\right) \quad (52)$$

$$u_r = -\frac{(1+\nu)}{E} \left\{ (1-2\nu)p_0 r + (p_0 - p) \frac{a^2}{r} \right\} \quad (53)$$

where K and a are the bulk modulus and radius of liquid inclusion. E and ν are Young's modulus and Poisson's ratio of the elastic matrix.

Like the derivation process of the analytical solutions for the 2D liquid inclusion problem, the analytical solutions of a spherical liquid inclusion under the remote triaxial pressure in 3D problem can also be obtained, and the expressions of inner pressure, radial displacement and stress are given as

$$p = \frac{\frac{3K(1+\nu)}{E} \left(\frac{1}{2} + \frac{1-2\nu}{1+\nu} \right)}{1 + \frac{3K(1+\nu)}{2E}} p_0 \quad (54)$$

$$u_r = \frac{(1+\nu)r}{E} \left\{ \frac{a^3}{2r^3} p - \left(\frac{a^3}{2r^3} + \frac{1-2\nu}{1+\nu} \right) p_0 \right\} \quad (55)$$

$$\sigma_r = -\frac{a^3}{r^3} p - \left(1 - \frac{a^3}{r^3} \right) p_0 \quad (56)$$

The details of the derivation can be found in Appendix B.

In the calculation, the polynomial orders and knot vectors of the IGABEM are shown in Table 1. The geometry and initial control points of the liquid inclusion are shown in Fig. 4. We set the Young's modulus and Poisson's ratio as 100000 and 0.3 respectively. The radius a is 1, and the remote pressure p_0 is 100. The radial displacement and stress fields of the matrix for 2D problem are illustrated in Figs. 5 and 6. The part (a) means the numerical solutions and the part (b) represents the analytical solutions. It can be seen that the results obtained by IGABEM are in good agreement with those by analytical method. To be more specific, the results of inner pressure of liquid inclusion and the radial displacement, stress at $r = 2$ for 2D problem are listed in Tables 2–4. And the 3D results at $r = 2$ are shown in Tables 5–7. In these tables, the numerical results, the analytical solutions and the relative errors between them under different dimensionless coefficient K/E are computed. Obviously, the results computed by IGABEM are in good agreement with analytical solutions. In addition, with the increment of the K/E , the inner pressure increases while the radial displacement decreases, indicating the liquid inclusion can reduce the deformation at the interface.

4.2. Liquid inclusion under uniaxial remote load

In this section, the mechanical properties of the elastic matrix with a single 2D or 3D liquid inclusion under uniaxial remote load is discussed. And the contents of 2D and 3D problems are illustrated in 4.2.1 and 4.2.2 respectively.

4.2.1. An elliptical liquid inclusion in the infinite plane

As shown in Fig. 7 (a), a single elliptical liquid inclusion in the infinite plane under remote uniaxial load p_0 is studied. In order to discuss the elastic properties and compare them with the contents in [6], we use the same settings as follows:

$$\begin{cases} a = c(R + 1/R) \\ b = c(R - 1/R) \end{cases} \quad (57)$$

where a and b are the major axis and minor axis respectively. c is half of the distance between two focal points. R is the shape parameter. Especially, when R approaches 1, the shape of liquid inclusion tends to a crack. When R is large, the shape is close to a circular. The geometry and the initial control points under $R = 3$ are illustrated in Fig. 7 (b). The orders and knot vectors are shown in Table 1.

Meanwhile, we define the dimensionless parameter as the same as that in [6],

$$K' = \frac{Kc^2}{\pi Gab} \quad (58)$$

It should be noted that in this part we use uniaxial remote loading $p_0 = -1$ in y -direction. The shear modulus of the matrix is 100000 and the Poisson's ratio is 0.3. At first, we compute the elastic field around the elliptical liquid inclusion when $K' = 1$ and $R = 3$. The stress field in x and y directions are illustrated in Fig. 8 (a) and (b). The maximum values in x -direction is 1.495 and in y -direction is -2.275, which are observed at the endpoints of the major and minor axes. Notice that the maximum stress appears in y -direction, so in the next discussion, we focus on the stress in y -direction. In Figs. 9 and 10, it should be noted that the red

lines represent the results obtained by the method in [6], and the marked points are computed by the IGABEM. The results show that the solutions obtained by IGABEM match analytical solutions very well. In Fig. 9, the ratio σ_y/p_0 along the x -axis are computed for different values of K' when $R = 2$. It is obvious that σ_y/p_0 decreases when the point is far away from the interface. It can also be seen that with the increase of the dimensionless parameter K' , σ_y/p_0 decrease obviously, but the effect of bulk modulus decrease with the increase of K' , indicating that the stress around the liquid inclusion is reduced to some extent.

Figs. 10 and 11 show the ratio $\Delta p/p_0$ and stress concentration factor $CF = \sigma_y/p_0$ under different shape parameters R and different dimensionless parameters K' . In Fig. 10, the normalized pressure increases with the increase of K' . When $K' \geq 1$, it can be seen that the ratio $\Delta p/p_0$ reaches the maximum around $R = 1.4$. After that, the ratio $\Delta p/p_0$ decreases with the increase of R . In Fig. 11, it is obvious that with the increase of K' , the stress concentration decreases under different shape parameters R , especially when R approaches 1. However, when K' is large, the effect of the bulk modulus is not significant. The results show that the concentration factor is reduced to some extent by liquid inclusion. When $R \geq 3$, the results are very close for the same value of since the shape of the liquid inclusion is close to a circle.

4.2.2. Liquid inclusion in the 3D problem. In this section, the mechanical properties of the 3D matrix with liquid inclusion under uniaxial remote load is studied. The polynomial orders and knot vectors are shown in Table 1, and the initial control points of the liquid inclusion are illustrated in Fig. 12. The Young's modulus and the Poisson's ratio of the matrix are 100000 and 0.3, respectively. First, for a remote load $p_0 = -1$ along z -axis, we study the stress field around the spherical liquid inclusion of radius 1. The stress fields in z -direction on the liquid-matrix interface and around elastic matrix in the first quadrant are shown in Fig. 13. In part (a), it can be seen that the stress reaches the maximum in $z = 0$ plane. The part (b) shows that the stress changes greatly only near the liquid inclusion.

Next, we study how the bulk modulus of liquid inclusions under different shapes affects the inner pressure and the stress concentration factor. We set three kinds of aspect ratios as 1:1:0.5, 1:1:1 and 1:1:1.5. By changing the bulk modulus, the inner pressure and stress concentration factor $CF = \sigma_z/p_0$ are calculated, and the results are illustrated in Fig. 14. Obviously, with the increase of the bulk modulus of the liquid inclusion, the pressure increases and the stress concentration factor decreases. Especially, when $-1 \leq \log(K/E) \leq 1$, the changes of the pressure and the CF are obvious, indicating that this region is the most sensitive to compressibility. However, when bulk modulus is outside this region, the results tend to change slowly or even to be a constant. The cases where the bulk modulus is too large or too small compared to Young's modulus are called incompressible and infinite compressible, and are two simplifications in some researches [8]. In addition, through the comparison of liquid inclusions with different shapes, it can be seen that when the aspect ratio is 1:1:0.5, the bulk modulus has the most significant effect on reducing the stress concentration factor, while the others are not obvious. Therefore, when the minor axis is parallel to the load axis, the stress concentration factor can be reduced significantly.

Furthermore, the relationship between the Young's modulus of the elastic matrix and the bulk modulus of the liquid inclusion is discussed. Let the Young's modulus be 1×10^4 , 1×10^6 and 1×10^8 . The bulk modulus is changed to obtain the inner pressure and stress concentration factor as shown in Fig. 15. One can see that there is a region ($2 \leq \log(K) \leq 8$) where the sensitivity to the compressibility is significant. It can also be seen that the CFs keep the same when the bulk modulus is too large or too small compared to Young's modulus, indicating that the stress concentration factor is independent of the Young's modulus in the incompressible and the infinite compressible cases. In addition, the region sensitive to the compressibility is obviously related to the Young's modulus, that is, when the Young's modulus changes, the region also

changes.

4.3. Randomly distributed liquid inclusions in plane 2D/3D elastic matrix

In this part, we will study the effective elastic modulus and Poisson's ratio of the matrix with randomly distributed liquid inclusions by using the RVE. To obtain the model of randomly distributed liquid inclusions, the random function in MATLAB software is employed to generate random distributions of liquid inclusions. But if we do not use specific skills, there are some inclusions that overlap. To avoid the overlap of the inclusions, we adopt the oriented bounding box (OBB) based on separation axis theorem (SAT), which is the idea of physics engine handling the collision. The SAT means that for any line in the area, if the projections of two convex polyhedrons on the line do not intersect, then the line can be defined as the separation axis of the two convex polyhedrons. If the separation axis exists, the two convex polyhedrons will not intersect. One should note that the enveloping box formed by the control points of the liquid inclusion is the OBB surrounding the inclusion. Based on SAT, we can easily generate the numerical models with random distributions of different shapes and positions, as shown in Fig. 16, where the area of liquid inclusions is 0.5 for 2D problem and the volume of liquid inclusions is 10 for 3D problem. The polynomial orders and vectors of the 2D outer boundary, liquid-matrix interface and 3D liquid-matrix interface are listed in Table 1, and those of the 3D outer boundary are listed in Table 8. The initial control points for 2D and 3D random inclusions are illustrated in Fig. 17.

In numerical implementation, the Young's modulus and Poisson's ratio of the matrix are 100000 and 0.3, respectively. The side length L of square or cube is 10. For 2D plane strain problem, we set the boundary conditions as follows:

$$\begin{cases} u_x = 0, x = -L/2 \\ u_y = 0, y = -L/2 \\ F_y = -100, y = L/2 \end{cases} \quad (59)$$

The effective Young's modulus \bar{E} , effective Poisson's ratio $\bar{\nu}$ are defined as

$$\bar{\nu}' = -\bar{u}_y|_{y=L/2} / \bar{u}_x|_{x=L/2} \bar{E} = \bar{u}_x|_{x=L/2} / L \quad (60)$$

$$\bar{E} = -(1 - \bar{\nu}^2)F_y / \bar{E}\bar{\nu} = \bar{\nu}' / (1 + \bar{\nu}') \quad (61)$$

where \bar{u}_x and \bar{u}_y are the average displacements in x and y directions, respectively. Similarly, the boundary conditions for 3D problem are as follows:

$$\begin{cases} u_x = 0, x = L/2 \\ u_y = 0, y = L/2 \\ u_z = 0, z = -L/2 \\ F_z = -100, z = L/2 \end{cases} \quad (62)$$

And the effective Young's modulus \bar{E} , effective Poisson's ratio $\bar{\nu}_{xz}$ and $\bar{\nu}_{yz}$ are defined as:

$$\bar{E} = \bar{u}_z / L\bar{E} = F_z / \bar{E} \quad (63)$$

$$\bar{\nu}_{xz} = -\bar{u}_x|_{x=-L/2} / \bar{u}_z|_{z=L/2} \bar{\nu}_{yz} = -\bar{u}_y|_{y=-L/2} / \bar{u}_z|_{z=L/2} \quad (64)$$

where \bar{u}_x , \bar{u}_y , \bar{u}_z are the average displacements in x , y and z directions.

To show the effect of the liquid inclusions on the elastic field of the matrix, we compute the displacement and Mises stress fields in Fig. 16 (a) by IGABEM, and the results are illustrated in Fig. 18. The bulk modulus of the liquid inclusion is equal to the Young's modulus here.

Part (a) and part (b) show the displacements in x and y directions, respectively. Part (c) and part (d) show the Mises stress fields of the elastic matrix with random liquid inclusions and holes, respectively. The larger Mises stresses are observed at the endpoints of the major axis. The maximum Mises stress in part (d) is 679.059 and in part (c) is 438.198. The Mises fields of the interface of the randomly distributed liquid inclusions and holes for Fig. 16 (b) are illustrated in Fig. 19, where the bulk modulus of the liquid inclusion is equal to the Young's modulus of the matrix. The maximum Mises stress in part (a) is 317.763 and in part (b) is 261.309. The Mises stress is significantly reduced in both 2D and 3D problems, indicating that the liquid inclusion can significantly reduce the maximum Mises stress.

In addition, the effective Young's modulus \bar{E} and Poisson's ratio $\bar{\nu}$ for 2D problem are shown in Fig. 20. The effective elastic modulus \bar{E} , Poisson's ratio $\bar{\nu}_{xz}$ and $\bar{\nu}_{yz}$ for 3D problem are illustrated in Fig. 21. From Figs. 20 (a) and 21 (a), it can be seen that the effective Young's modulus decreases with the increase of porosity ratio, but increases with the increase of K/E , indicating that the liquid inclusion can strengthen the stiffness of the elastic matrix. In Fig. 20 (b), we can see that when $K/E = 0$, the effective Poisson's ratio decreases with the increase of volume fraction, while in other cases, the effective Poisson's ratio increases. There is a slight difference in 3D problem, in both cases $K/E = 0$ and $K/E = 0.1$, the effective Poisson's ratio decreases as shown in Fig. 21 (b) and (c).

5. Conclusion

In this paper, the mechanical properties of 2D and 3D elastic matrices containing liquid inclusions have been studied by the IGABEM. The method only discretizes the boundary, has no geometric error and high accuracy. To verify the accuracy of the IGABEM, a circle and a spherical liquid inclusion in the infinite domain under remote uniform load were studied first, and the comparison between the analytical solutions and numerical solutions were given. One can see that the results obtained by IGABEM are in good agreement with the analytical solutions.

Next, we studied the mechanical properties of the liquid inclusion problem under uniaxial load. The liquid inclusion can reduce the stress concentration factor. Especially under the remote load, when the minor axis is parallel to the direction of load, the effect of the liquid inclusion is significant. When bulk modulus is close to the Young's modulus, the sensitivity to the compressibility is highest. However, when the bulk modulus is too large or too small comparing to Young's modulus, the influence of the compressibility is weakened.

Finally, we studied the effective Young's modulus and effective Poisson's ratio for 2D and 3D problems. The results show that the effective Young's modulus decreases with the increase of volume fraction in both 2D and 3D cases. When $K/E = 0$ or the ratio is small, the effective Poisson's ratio decreases while in other cases, the effective Poisson's ratio increases. In the study of the effect of bulk modulus, it is found that with the increment of the ratio K/E , both the effective Young's modulus and effective Poisson's ratio increase. Therefore, the liquid inclusion can strength the effective mechanical properties.

Declaration of Competing Interest

The authors declare no conflict of interest.

Acknowledgements

The research is supported by the National Natural Science Foundation of China (11972085, 11672038).

Appendix A

The fundamental solutions for the two-dimensional plane strain problems are shown as [47]:

$$\begin{cases} U_{ij}^* = \frac{1}{8\pi\mu(1-\nu)} \left[(3-4\nu)\ln\frac{1}{r}\delta_{ij} + r_j r_i \right] \\ T_{ij}^* = -\frac{1}{4\pi(1-\nu)r} \left\{ \frac{\partial r}{\partial n} [(1-2\nu)\delta_{ij} + 2r_j r_i] + (1-2\nu)(n_i r_j - n_j r_i) \right\} \end{cases}$$

and the Jacobian for the transformation from the physical space to parametric space is given as:

$$|J_1| = \frac{d\Gamma}{d\xi} = \sqrt{(dx/d\xi)^2 + (dy/d\xi)^2}$$

and the Jacobian from parametric space to Gaussian space is

$$|J_2| = (\xi_2 - \xi_1) / 2$$

The D_{kij} and S_{kij} in 2D problem are shown as follows [50]:

$$\begin{cases} D_{kij} = \frac{1}{4\pi(1-\nu)r} [(1-2\nu)(\delta_{ik}r_j + \delta_{jk}r_i - \delta_{ij}r_k) + 2r_i r_j r_k] \\ S_{kij} = \frac{\mu}{2\pi(1-\nu)r^2} \left\{ 2\frac{\partial r}{\partial n} [(1-2\nu)\delta_{ij}r_k + \nu(r_j\delta_{ik} + r_i\delta_{jk}) - 4r_i r_j r_k] \right\} \\ + \frac{\mu}{2\pi(1-\nu)r^2} \{ 2\nu(n_i r_j r_k + n_j r_i r_k) \} \\ + \frac{\mu}{2\pi(1-\nu)r^2} \{ (1-2\nu)(2n_k r_i r_j + n_j \delta_{ik} + n_i \delta_{jk}) - (1-4\nu)n_k \delta_{ij} \} \end{cases}$$

For 2D problem, the stress on the boundary can be computed just as for 3D problem. At first, we get the vector in local coordinate system as shown in Fig. 22:

$$\hat{\mathbf{r}} = \hat{x}\hat{\mathbf{e}}_1 + \hat{y}\hat{\mathbf{e}}_2$$

with

$$\hat{\mathbf{e}}_1 = \mathbf{n}, \hat{\mathbf{e}}_2 = \frac{\mathbf{m}}{|\mathbf{m}|}$$

where \mathbf{n} is the normal at the boundary, and \mathbf{m} is defined as

$$\mathbf{m} = \frac{d\mathbf{r}}{d\xi}$$

Therefore, the transformation matrix is

$$A = \begin{bmatrix} \hat{\mathbf{e}}_1 \\ \hat{\mathbf{e}}_2 \end{bmatrix}$$

The local strain can be obtained by

$$\hat{\varepsilon}_{22} = \frac{\partial \hat{u}_2}{\partial \xi} \frac{\partial \xi}{\partial \hat{x}_2} = A_{2j} \frac{\partial u_j}{\partial \xi} \frac{\partial \xi}{\partial \hat{x}_2}$$

with

$$\frac{\partial \xi}{\partial \hat{x}_2} = \frac{1}{|\mathbf{m}|}$$

The stress in local coordinate system can be written as

$$\begin{cases} \hat{\sigma}_{11} = \hat{t}_1 \\ \hat{\sigma}_{12} = \hat{t}_2 \\ \hat{\sigma}_{22} = \frac{E}{1-\nu^2} \hat{\varepsilon}_{22} + \frac{\nu}{1-\nu} \hat{t}_1 \end{cases}$$

Finally, the stress in global coordinate system can be obtained by

$$\sigma_{ij} = A_{ki} A_{nj} \hat{\sigma}_{kn}$$

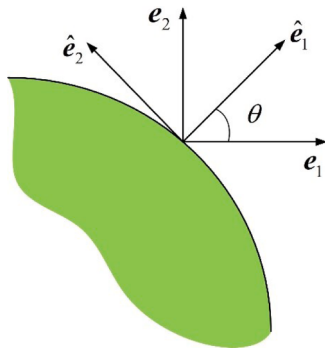


Fig. 22. Local coordinate system.

Appendix B

The analytical solution of a hollow sphere under uniform pressure are shown as

$$\sigma_r = -\frac{\frac{b^3}{r^3} - 1}{\frac{b^3}{a^3} - 1} p - \frac{1 - \frac{a^3}{r^3}}{1 - \frac{a^3}{b^3}} p_0 \quad (1)$$

$$u_r = \frac{(1 + \nu)r}{E} (A(r)p - B(r)p_0) \quad (2)$$

where

$$A(r) = \frac{\frac{b^3}{2r^3} + \frac{1-2\nu}{1+\nu}}{\frac{b^3}{a^3} - 1}, B(r) = \frac{\frac{a^3}{2r^3} + \frac{1-2\nu}{1+\nu}}{1 - \frac{a^3}{b^3}} \quad (3)$$

a and b are the inner and outer radius respectively. Under the assumption of small deformation, we can get the variation of the liquid volume as

$$\Delta V = \frac{4\pi(a + u_r)^3}{3} - \frac{4\pi a^3}{3} = 4\pi a^2 u_a \quad (4)$$

With the relation between pressure and volume variation,

$$-K \frac{\Delta V}{V} = p \quad (5)$$

we can get the pressure of the liquid inclusion from Eqs. (2), (4) and (5) as follows:

$$p = \frac{\frac{3K(1+\nu)}{E} B(a)}{1 + \frac{3K(1+\nu)}{E} A(a)} p_0 \quad (6)$$

When the outer radius approaches infinite, Eq. (3) can be written as:

$$A = \frac{a^3}{2r^3}, B = \frac{a^3}{2r^3} + \frac{1-2\nu}{1+\nu} \quad (7)$$

Substituting Eq. (7) into Eqs. (2) and (6), we can get

$$u_r = \frac{(1 + \nu)r}{E} \left\{ \frac{a^3}{2r^3} p - \left(\frac{a^3}{2r^3} + \frac{1-2\nu}{1+\nu} \right) p_0 \right\} \quad (8)$$

and

$$p = \frac{\frac{3K(1+\nu)}{E} \left(\frac{1}{2} + \frac{1-2\nu}{1+\nu} \right)}{1 + \frac{3K(1+\nu)}{2E}} p_0 \quad (9)$$

and Eq. (1) becomes

$$\sigma_r = -\frac{a^3}{r^3} p - \left(1 - \frac{a^3}{r^3} \right) p_0 \quad (10)$$

References

- [1] Gratter JP, Jenatton L. Deformation by solution-deposition, and re-equilibration of fluid inclusions in crystals depending on temperature, internal pressure and stress. *J Struct Geol* 1984;6(1):189–200.
- [2] Poulet T, Veveakis M. A viscoplastic approach for pore collapse in saturated soft rocks using REDBACK: an open-source parallel simulator for Rock mEchanics with Dissipative feedBACKs. *Comput Geotech* 2016;74:211–21.
- [3] Campás O, Mammoto T, Hasso S, Sperling RA, O'Connell D, Bischof AG, et al. Correction: Corrigendum: Quantifying cell-generated mechanical forces within living embryonic tissues. *Nat Methods* 2014;11(3):349.
- [4] Miriyev A, Stack K, Lipson H. Soft material for soft actuators. *Nat Commun* 2017;8(1):596.
- [5] Owuor PS, Hiremath S, Chipara AC, Vajtai R, Lou J, Mahapatra DR, et al. nature inspired strategy to enhance mechanical properties via liquid reinforcement. *Adv Mater Interfaces* 2017;4(16):1700240.
- [6] Wu J, Ru CQ, Zhang L. An elliptical liquid inclusion in an infinite elastic plane. *Proc Royal Soc A: Math Phys Eng Sci* 2018;474(2215):20170813.
- [7] Eshelby JD. The determination of the elastic field of an ellipsoidal inclusion, and related problems. *Proc Royal Soc Lond. Ser A, Math Phys Sci* 1957;241(1226):376–96.
- [8] Chen X, Li M, Yang M, Liu S, Genin GM, Xu F, et al. The elastic fields of a compressible liquid inclusion. *Extrem Mech Lett* 2018;22:122–30.
- [9] Wang YH, Henann DL. Finite-element modeling of soft solids with liquid inclusions. *Extrem Mech Lett* 2016;9:147–57.
- [10] Seifi S, Park HS. Computational modeling of electro-elasto-capillary phenomena in dielectric elastomers. *Int J Solids Struct* 2016;87:236–44.
- [11] Yao Z, Kong F, Wang H, Wang P. 2D Simulation of composite materials using BEM. *Eng Anal Bound Elem* 2004;28(8):927–35.
- [12] Rana SK, Jena A. A BEM formulation of two dimensional steady state heat conduction in exchanger tubes of arbitrary cross sections. *Int J Heat Mass Transf* 2017;106:195–211.
- [13] Gao XW, Zhang C, Sladek J, Sladek V. Fracture analysis of functionally graded materials by a BEM. *Compos Sci Technol* 2008;68(5):1209–15.
- [14] Zheng C, Zhao W, Gao H, Du L, Zhang Y, Bi C. Sensitivity analysis of acoustic eigenfrequencies by using a boundary element method. *J Acoust Soc Am* 2021;149(3):2027–39.
- [15] Zheng C, Bi C, Zhang C, Gao H, Chen H. Free vibration analysis of elastic structures submerged in an infinite or semi-infinite fluid domain by means of a coupled FE-BE solver. *J Comput Phys* 2018;359:183–98.
- [16] Huang Q, Zheng X, Yao Z. Boundary element method for 2D solids with fluid-filled pores. *Eng Anal Bound Elem* 2011;35(2):191–9.
- [17] Ma H, Zhou J, He D. Eigenstrain formulation of boundary integral equations for modeling 2D solids with fluid-filled pores. *Eng Anal Bound Elem* 2019;104:160–9.
- [18] Krichen S, Liu L, Sharma P. Liquid inclusions in soft materials: capillary effect, mechanical stiffening and enhanced electromechanical response. *J Mech Phys Solids* 2019;127:332–57.
- [19] Liang H, Cao Z, Dobrynin A. Molecular dynamics simulations of the effect of elastocapillarity on reinforcement of soft polymeric materials by liquid inclusions. *Macromolecules* 2016;49:7108–15.
- [20] Shafiro B, Kachanov M. Materials with fluid-filled pores of various shapes: Effective elastic properties and fluid pressure polarization. *Int J Solids Struct* 1997;34(27):3517–40.
- [21] Style RW, Boltynskiy R, Allen B, Jensen KE, Foote HP, Wetzlauer JS, et al. Stiffening solids with liquid inclusions. *Nat Phys* 2015;11(1):82–7.
- [22] Style RW, Wetzlauer JS, Dufresne ER. Surface tension and the mechanics of liquid inclusions in compliant solids. *Soft Matter* 2015;11(4):672–9.
- [23] Hughes TJR, Cottrell JA, Bazilevs Y. Isogeometric analysis: CAD, finite elements, NURBS, exact geometry and mesh refinement. *Comput Meth Appl Mech Eng* 2005;194(39):4135–95.
- [24] Cottrell JA, Reali A, Bazilevs Y, Hughes TJR. Isogeometric analysis of structural vibrations. *Comput Meth Appl Mech Eng* 2006;195(41–43):5257–96.
- [25] Yang HS, Dong CY, Wu YH. Postbuckling analysis of multi-directional perforated FGM plates using NURBS-based IGA and FCM. *Appl Math Model* 2020;84:466–500.
- [26] Politis C, Ginnis AI, Kaklis PD, Belibassakis K, Feurer C. An isogeometric BEM for exterior potential-flow problems in the plane. In: Proceedings of the 2009 SIAM/ACM joint conference on geometric and physical modeling; 2009. p. 349–54.
- [27] Belibassakis KA, Gerostathis TP, Kostas KV, Politis CG, Feurer C. A novel BEM-isogeometric method with application to the wavemaking resistance problem of bodies at constant speed. In: Proceedings of the international maritime association Mediterranean conference (IMAM 2009); 2009.
- [28] Wang L. Integration of CAD and boundary element analysis through subdivision methods. *Comput Ind Eng* 2009;57(3):691–8.
- [29] Takahashi T, Matsumoto T. An application of fast multipole method to isogeometric boundary element method for Laplace equation in two dimensions. *Eng Anal Bound Elem* 2012;36(12):1766–75.
- [30] Simpson RN, Bordas SPA, Trevelyan J, Rabczuk T. A two-dimensional isogeometric boundary element method for elastostatic analysis. *Comput Meth Appl Mech Eng* 2012;209–212:87–100.
- [31] Simpson RN, Bordas SPA, Lian H, Trevelyan J. An isogeometric boundary element method for elastostatic analysis: 2D implementation aspects. *Comput Struct* 2013;118:2–12.
- [32] Sun Y, Trevelyan J, Hattori G, Lu C. Discontinuous isogeometric boundary element (IGABEM) formulations in 3D automotive acoustics. *Eng Anal Bound Elem*, 105; 2019, p. 303–11.
- [33] Zang Q, Liu J, Ye W, Lin G. Isogeometric boundary element for analyzing steady-state heat conduction problems under spatially varying conductivity and internal heat source. *Comput Math Appl* 2020;80(7):1767–92.
- [34] Peng X, Atroshchenko E, Kerfriden P, Bordas SPA. Isogeometric boundary element methods for three dimensional static fracture and fatigue crack growth. *Comput Meth Appl Mech Eng* 2017;316:151–85.
- [35] Sun SH, Yu TT, Nguyen TT, Atroshchenko E, Bui TQ. Structural shape optimization by IGABEM and particle swarm optimization algorithm. *Eng Anal Bound Elem*, 88; 2018, p. 26–40.
- [36] Wu YH, Dong CY, Yang HS, Sun FL. Isogeometric symmetric FE-BE coupling method for acoustic-structural interaction. *Appl Math Comput* 2021;393:125758.
- [37] Yildizdag ME, Ardic IT, Kefal A, Ergin A. An isogeometric FE-BE method and experimental investigation for the hydroelastic analysis of a horizontal circular cylindrical shell partially filled with fluid. *Thin-Walled Struct* 2020;151:106755.
- [38] Guiggiani M, Casalini P. Direct computation of Cauchy principal value integral in advanced boundary elements. *Int J Numer Methods Eng* 1987;24:1711–20.
- [39] Telles JC. A self-adaptive coordinate transformation for efficient numerical evaluation of general boundary element integrals. *Int J Numer Methods Eng* 1987;24:959–73.
- [40] Gong YP, Dong CY, Qin XC. An isogeometric boundary element method for three dimensional potential problems. *J Comput Appl Math* 2017;313:454–68.
- [41] Gao XW. An effective method for numerical evaluation of general 2D and 3D high order singular boundary integrals. *Comput Meth Appl Mech Eng* 2010;199(45):2856–64.
- [42] Yang HS, Dong CY, Wu YH. Non-conforming interface coupling and symmetric iterative solution in isogeometric FE-BE analysis. *Comput Meth Appl Mech Eng* 2021;373:113561.
- [43] Rokhlin V. Rapid solution of integral equations of classical potential theory. *J Comput Phys* 1985;60(2):187–207.
- [44] Kurz S, Rain O, Rjasanow S. The adaptive cross-approximation technique for the 3D boundary-element method. *IEEE Trans Magn* 2002;38:421–4.
- [45] Sun FL, Dong CY, Wu YH, Gong Y. Fast direct isogeometric boundary element method for 3D potential problems based on HODLR matrix. *Appl Math Comput* 2019;359:17–33.
- [46] Piegl L, Tiller W. The NURBS Book. 2nd. Springer; 1997.
- [47] Brebbia CA, Dominguez J. Boundary elements: an introductory course. Computational Mechanics Publications; 1992.
- [48] Dong CY, Lo S, Cheung Y. Interaction between coated inclusions and cracks in an infinite isotropic elastic medium. *Eng Anal Bound Elem* 2003;27:871–84.
- [49] Johnson RW. Higher order B-spline collocation at the Greville abscissae. *Appl Numer Math* 2005;52(1):63–75.
- [50] Lian H, Kerfriden P, Bordas SPA. Shape optimization directly from CAD: an isogeometric boundary element approach using T-splines. *Comput Meth Appl Mech Eng* 2017;317:1–41.